EXPERIMENTS ON THE THERMAL PERFORMANCE OF RIBBON PARACHUTES

C. J. SCOTT E. R. G. ECKERT

UNIVERSITY OF MINNESOTA

TECHNICAL REPORT No. AFFDL-TR-64-192

MAY 1965

AIR FORCE FLIGHT DYNAMICS LABORATORY RESEARCH AND TECHNOLOGY DIVISION AIR FORCE SYSTEMS COMMAND WRIGHT-PATTERSON AIR FORCE BASE, OHIO

NOTICES

ATRIBUTION TO SERVICE THE WAS BIT AS INCLUDENT FOR LEVEL FOR UNION THE PROBLEM TO SERVICE THE SERVICE THE SERVICE TO SERVICE THE SERVICE T

When Government drawings, specifications, or other data are used for any purpose other than in connection with a definitely related Government procurement operation, the United States Government thereby incurs no responsibility nor any obligation whatsoever; and the fact that the Government may have formulated, furnished, or in any way supplied the said drawings, specifications, or other data, is not to be regarded by implication or otherwise as in any manner licensing the holder or any other person or corporation, or conveying any rights or permission to manufacture, use, or sell any patented invention that may in any way be related thereto.

Qualified users may obtain copies of this report from Defense Documentation Center.

Foreign announcement and dissemination of this report is not authorized.

The distribution of this report is limited because the report contains technology identifiable with items on the strategic embargo lists excluded from export and re-export under U. S. Export Control Act of 1949 (63 Stat. 7) as amended (50 U.S.C. App. 2020.2031) as implemented by AFR 400-10.

Copies of this report should not be returned to the Research and Technology Division unless return is required by security considerations, contractual obligations, or notice on a specific document.

AFFDL-TR-64-192

EXPERIMENTS ON THE THERMAL PERFORMANCE OF RIBBON PARACHUTES

C. J. SCOTT E. R. G. ECKERT

UNIVERSITY OF MINNESOTA

FOREWORD

This report summarizes the work done by the Heat Transfer Laboratory, Department of Mechanical Engineering, University of Minnesota, during a research program sponsored by the Recovery and Crew Station Branch of the Air Force Flight Dynamics Laboratory under Contract AF33(657)11688, Project No. 6065, Task No. 606503. The manuscript was released by the authors September 1964 for publication as an RTD Technical Report. The contract's technical project monitor was C. A. Babish lII of the Air Force Flight Dynamics Laboratory. E. R. G. Eckert served as principal investigator of the contract at the University of Minnesota.

The report covers work conducted from July 1963 through September 1964.

The authors wish to thank other persons on the staff of the University of Minnesota who have contributed to various phases of the work. In particular, special acknowledgements are due to Dr. R. Olson for his design work and Mr. V. Jonsson, who programmed the data reduction procedures. Appreciation is also extended to Messrs. K. Krall, J. Lloyd, and B. Williams for their precise work during the operation of the pressurized subsonic wind tunnel and assistance in the data reduction and analysis.

This technical report has been reviewed and is approved.

Vehicle Equipment Division

AF Flight Dynamic Laboratory

ABSTRACT

Experimental heat transfer studies were conducted on full scale ribbons of flat circular type parachutes having a geometric porosity of 20.5 percent. A pressurized subsonic wind tunnel served as the flow facility. The average approach flow velocity was 134 feet per second. The measurements were made in the Reynolds number range of one million to ten million, where the Reynolds number is based on the ribbon width of 2.1 inches and on the velocity and temperature of the flow in the slots between the ribbons. The pressure ratio applied to the ribbon was varied from 1.4 to 26.3. Using a transient energy balance, local and average heat transfer data were obtained and compared with available analyses.

TABLE OF CONTENTS

SECTION		1' A Gb)
I	INTRODUCTION	1.
	A. Large Scale Phonomona	2
	B. Small Scale Phenomena	3
ΤŢ	EXPERIMENTAL EQUIPMENT AND PROCEDURES	6
	A. Facility	6
	B. Experimental Model	8
111	EXITERIMENTAL STUDIES	1.0
	A. Uniformity of Approach Flow	10
	B. Ribbon Pressure Ratios	1.1.
	C. Ribbon Surface Pressure Distribution	11,
	D. Heat Transfer Measurements	17
	1. Forward-Pacing Surface	17
	(a) Recovery Temperature Distribution	17
	(b) Heat Transfer Runs	18
	2. Rearward Facing Surface	22
	(a) Recovery Temperature Distribution	22
	(b) Heat Transfer Huns	23
IA	CONCLUCTONS	26
	REFERENCES	27
	A DDGWHYTV - A	1.1.4

٧

TLLUSTRATIONS

FIGURE		rA(3)
1	Sketch of Ribbon Parachute Flow Patterns	29
2	Photograph of the Experimental Apparatus Showing the Pressurized Subsonic Wind Tunnel	30
3	Sketch of the Test Section of the Pressurized Subsonic Wind Tunnel	31
L,	Ribbon Farachute Model Installed in the Wind Tunnel (a) Side View Through Window (b) Rear View Looking Upstream	32
5	Sketch of Ribbon Parachute Model Showing Construction and Instrumentation Details	33
6	Shadowgraph Photographs of the Flow Downstream of the Slots	34
7	Approach Flow Velocity Distribution Rake	35
8	Uniformity of Approach Flow Velocities	36
9	Variation of Downstream Pressures with Ribbon Reynolds Number	37
10	Pressure Ratios Across the Ribbon Versus Ribbon Reynolds Number	37
11	Typical Surface Pressure Distributions on the Center Ribbon	38
12	The Shift in the Stagnation Point Location as Indicated by Surface Pressure Measurements	39
13	Ribbon Surface Velocity Distributions	40
14.	Stagnation Point Velocity Gradients Calculated from Surface Static Pressure Measurements	1,1
1.5	Recovery Temperature Ratios for the Upstream Side	42
16	Upstream Stagnation Point Heat Transfer Coefficients	43
17	Correlation of Upstream Stagnation Point Heat Transfer and Pressure Data with Laminar Stagnation Point Boundary Layer Analysis	1414
18	Distribution of Heat Transfer Coefficients on the Upstream Side	45
19	Average Heat Transfer Coefficients on the Upstream Side	46

ILLUSTRATIONS (concile)

FIGURE		PAGE
20.	Comparison of Present Results with Previous Experiments on Ribbon Parachute Heat Transfer	147
21	Recovery Temperature Ratios for the Downstream Side	$I_{\pm}\Omega$
2.2	Downstream Stagnation Point Heat Transfer Coefficients	49
23	Correlation of Downstream Stagnation Point Heat Transfer and Pressure Data with Isminar Stagnation Point Boundary Layer Analysis	50
2/4	Distribution of Heat Transfer Coefficients on the Downstream Side	51 and 52
25	Average Heat Transfer Coefficients on the Downstream Side	53
26	Comparison of Present Results with Previous Experiments on Ribbon Parachute Neat Transfer	54
27	Variation of Both Upstream and Downstream Stagnation Point Heat Transfer Rates with the Pressure Ratio Across the Ribbon	55
28	Heat Transfer Data at the Center of the Slot of a Ribbon Parachute of Fxaggerated Thickness	56
29	Mnergy Balance Notation	57
30	Typical Temperature Traces	63
31	Correlation of Heat Capacity Data for Iron	64
32	Extrapolation of Heat Transfer Coefficients to a Uniform Wall Temperature Condition	(55
33	Integration of the local Head Thomaster Values	((

NOMENCLATURE*

```
convective heat transfer area, ft2
Λ
         speed of sound, ft/see
a
         specific heat, Btu/1b_{\rm IR} - ^{\rm O}R
         width of parachute ribbon, "slat", ft
])
         convective heat transfer coefficient, Btu/hr-ft^2 - ^{\rm o}R
h
         thermal conductivity, Btu/hr-ft-OR
Μ
         Mach number
             Nusselt number based on stagnation conditions
Nu
         hx Nusselt number based on wall conditions
Nu
         absolute static pressure, lb<sub>1</sub>/in<sup>2</sup>
p
         rate of heat transfer per unit area, Btu/hr-ft2
q
         distance along ribbon from stagnation point, it.
                    Reynolds number based on slat width and sonic conditions in the slot
         slat half width, ft
         temperatures, or or oR
Т
         recovery temperature, or or
         thickness, ft
         external flow velocity outside boundary layer, ft/sec
\eta_{\kappa}
         undisturbed velocity approaching model, ft/sec
U_{\infty}
         density, 1bm/ft<sup>3</sup>
         time, hr
```

Superscripts

denotes sonic conditions calculated from the measured stagnation conditions, assuming an isentropic expansion to sonic velocity

Several symbols defined in the text and used but to be the specied included in this list.

NOMENCLATURE (cont'd)

rockeneraten baranister erren in der mennen bestemmen den en bing in die militer in die die die stemmen der die

Subscripts

:w	denotes adiabatic wall conditions, $q_{\overline{W}}^-$ O
avg	average value
D	conditions based on slat width D
exit	denotes conditions downstream of ribbon
1	denotes undisturbed conditions upstream of model
2	denotes conditions at the downstream stagnation point of the ribbon
m	refers to ribbon material
0	denotes stagnation conditions, also condition in settling chamber before wind tunnel contraction
stag	denotes conditions at the stagnation point
W	denotes local conditions at the surface of the test ribbon
8	denotes conditions at edge of boundary layer

I. INTRODUCTION

A growing interest in the use of parachutes for aerospace-vehicle recovery operations has directed attention to the aerodynamic heat transfer problems involved when high speed aerodynamic decelerators are employed. A variety of retardation devices have been proposed which satisfy such dynamic design requirements as filling time, opening shock, drag establishment and control and stability. However, as the flight Mach number is increased, a common problem, aerodynamic heating, is encountered. At the present time, there exists neither a fully predictive theory nor sufficient experimental data to permit reliable calculations of the heat rates involved in the several deceleration schemes (1).

In general, aerodynamic decelerators must possess a large drag-to-weight ratio and must be capable of being stored in a small volume.

Therefore, most proposed drag producing devices are relatively thin and flexible. In addition, dynamic stability requires venting or porosity.

As a result, most retardation techniques employ porous surfaces involving high temperature plastic, glass, or wire mesh cloth in conjunction with other venting techniques. The heat transfer to these elements of mesh is a common problem in parachute performance calculations. Alternately, experimental heat transfer data must be applied to a variety of situations.

The flow field associated with a parachute results from the interaction of the large-scale phenomena enveloping the complete body and the small-scale processes associated with the local flow about a single element in the mesh material itself. The large scale phenomena, (parachute shape and size, velocity, altitude) which vary with the particular design, are

Numbers enclosed by brackets refer to references.

generally involved with the aerodynamics of the problem and contribute end or boundary conditions (pressure ratio, Reynolds number) to the small-scale phenomena.

A. Large Scale Phenomena

The range of interests in the present study consists of altitudes from sea level up to 200,000 feet and flight Mach numbers ranging from 2 to 5. A concave hemisphere canopy is a typical shape considered for supersonic operations although specification of the exact geometry is not necessary. In previous work (2), it was felt that a good starting point for study of the large-scale phenomena was the simple concave hemisphere. This provides a flow amenable to analysis and experiment. The experimental results of Reference (3) indicate that at angular locations up to 75 degrees from the stagnation point, the static pressure on the upstream surface of the concave hemisphere is equal to the total pressure. This means that there is practically no flow near and parallel to the surface of the hemisphere except near the edge. Of course, in supersonic flow, a normal shock would stand ahead of the hemisphere and this would produce a completely subsonic flow regime inside of the concave hemisphere. In the absence of any chute porosity, the pressure on the upstream side of the chute is closely approximated by the total pressure behind the normal shock. In determining the pressure on the rearward (downstream) face of the chute, we are led to a base pressure phenomena described by H. H. Korst (4).

The discussion in the previous paragraph illustrates a technique for computing the pressures and hence the pressure ratio across a chute with no porosity. The analysis for the base pressure problem has been extended to the case of flow through the chute with small momentum only.

Since this last condition is rarely met in the case of practical parachute configurations, the pressure ratio across the chute openings must be found from experiment.

B. Small Scale Phenomena

A high temperature, high density flow is produced inside the canopy. This flow passes through the individual openings of the mesh. Heat is transferred from the hot gases to the mesh elements. Therefore, it is the distribution of heat flux to the surfaces of a mesh element which is of primary importance. The element is bounded on each side by an opening (slot) through which the oncoming flow passes. The typical ribbon (slat) may be considered as a flat plate aligned normal to the flow. The approaching flow may or may not separate upstream of the ribbon. This process has not been clearly defined. The flow passing through the slots exhibits properties which depend upon the overall applied pressure ratio. In most flight applications, the applied pressure ratio will be such that the flow in the slot may be considered as a sonic flow. Additional energy is available for further expansion of the stream as it emerges from the slot such that localized regions of supersonic flow will occur downstream of the slot. Between the supersonic jets emerging from the slot and the rearward facing wall of the ribbon, two regions are found. The first is a conventional free-shear layer in which the streamwise component of velocity diminishes from the value found in the jet to a nearzero condition. Adjacent to the shear layer there exists a small region of reverse flow. There is a circulating vortex in this region. The local pressure in the separation bubble is determined by the local base pressure phenomena (the flow issuing from the slot). The mean near-wake pressure which exists further downstream is determined by the gross geometry and the freestream Mach number. These two pressures are probably not equal.

Therefore, further recompression exists downstream of the jets issuing from the individual slots. The local base pressure behind an individual ribbon is therefore determined by the slot pressure ratio and the recompression process in the shear layers.

The distribution of heat flux over the surface of a single ribbon is of primary importance. A model which applies to the general heat exchange process between the shear layers and the rearward facing wall of the ribbon has been proposed by Korst (l_1) and Chapman (5). Related experiments are discussed in References (6) and (7).

Considering a single ribbon in the absence of adjacent ribbons, the heat flux increases from the "apparent" stagnation point value (at the center of the ribbon) to higher values toward the outer edge of the ribbon, according to laminar analysis. Experimental evidence (8) covering the forward face of such a ribbon confirms this distribution of heat flux and in addition, the variation of heat flux with pressure level (for a fixed velocity gradient). When several ribbons are grouped together in a manner simulating a ribbon parachute, the heat flux distribution on the front-facing surface of a typical ribbon is influenced by the presence of the adjacent ribbons (2). The heat flux also increases at locations away from the stagnation point but at a rate somewhat faster than a single ribbon. The increased heat flux near the edge of the ribbon appears to be due to a diminution in the thickness of the viscous layer adjacent to the ribbon slot. This diminution is produced by the interaction of the slot flow with the ribbon boundary layer.

Recent experiments (6,7) suggest that adjacent to the separation bubble, a laminar, boundary-layer-like flow exists along the rear surface and this serves as the major barrier to the exchange of energy between

the freestream and the surface. In the case of a flat plate aligned normal to the flow, this thin film exhibits the properties of a stagnation-point boundary layer of the laminar type. The heat transfer processes along the forward and rearward faces of the ribbon appear to be governed by a similar mechanism.

Experimentally (7), the magnitude of the heat fluxes to the forward face are found to be considerably larger than those of the rearward face. This is primarily due to the significant difference in pressure level which occurs between the front and rear surfaces. The specific value of the ratio of heat fluxes on the forward and rearward surfaces varies with the freestream unit Reynolds number since base pressure phenomena depend on the character of the shear layer (laminar, transitional or turbulent).

The greatest source of uncertainty in engineering calculations of the energy exchange process to the mesh elements lies in the determination of the convective heat flux as characterized by a heat transfer parameter Nu. In the present instance the heat transfer parameter is a function of Reynolds number, ${\rm Re}^{*}$, and the pressure ratio across the ribbon, ${\rm P_1/P_2}$. The inter-relationships between Nu, ${\rm Re}^{*}$, and ${\rm P_1/P_2}$ are sufficiently complex that they must be determined experimentally. It is convenient to define a Reynolds number based on the velocity and flow properties in the sonic orifice and the slat width

$$\operatorname{Re}_{D}^{*} = \frac{\rho^{*} a^{*} D}{\mu^{*}} \tag{1}$$

In the flight case the static temperature T_{∞} and pressure p_{∞} are determined by the flight altitude. A total pressure p_{0} and temperature T_{0} are determined once the flight Mach number is prescribed. Since the bow

shock is assumed to be normal, the total pressure behind the normal shock P_o^{\dagger} (inside of the canopy) is determined from P_o and M_{oo}^{\dagger} . The total density, behind the bow shock, is computed from P_o^{\dagger} , T_o and the proper equation of state. Finally, the sonic density and speed are determined from an isentropic expanison from P_o^{\dagger} , P_o^{\dagger} , to P_o^{\dagger} and P_o^{\dagger} . The superscript * refers to the slot condition where a sonic speed exists for supercritical pressure ratios. The viscosity P_o^{\dagger} is a known function of the temperature P_o^{\dagger} .

The heat transfer parameter Nu is based on the stagnation conditions of the approaching flow and relates the wall heat flux to the difference between the wall temperature $T_{\rm w}$ and the adiabatic wall temperature $T_{\rm aw}$.

$$Nu = \frac{hD}{k_o} = \frac{q}{T_{aw} - T_w} \cdot \frac{D}{k_o}$$
 (2)

Notice that $k_{\stackrel{\cdot}{0}}$ is the thermal conductivity of the air at the stagnation temperature.

II. EXPERIMENTAL EQUIPMENT AND PROCEDURES

A. Facility

The experimental facility used in the present experiments appears in the photograph of the experimental setup, Figure 2, and is also sketched in Figure 3. This facility is located at the University of Minnesota's Rosemount Research Center. Prior to modification, the wind tunnel was a conventional blowdown supersonic windtunnel (9). The 6 x 12-inch supersonic windtunnel was modified by removing the supersonic nozzle blocks and fabricating a new 6 x 8-inch subsonic test section. A quick-acting DeZurik valve

The present experimental procedure is to simulate the subsonic flow conditions behind the bow shock. The total pressure behind the normal shock is preperly simulated by the windtunnel stagnation pressure (see Section IIA).

was installed in the 6-inch inlet pipe. The opening time of this valve is slightly less than one second, which is of importance when transient heat transfer measurements are made. A series of five perforated plates were placed at 11-inch intervals inside the 18-inch diameter stilling chamber and a 16-mesh screen was inserted between the flanges at the downstream end of this chamber to even out the flow. The plates and screen had a porosity of about 54 percent. Tests reported by Baines and Peterson (10) indicated that this is an optimum porosity for flattening out non-uniform velocity profiles.

A short round-to-rectangular contraction with an area ratio of 3.2 followed the stilling chamber, and the supersonic nozzle blocks normally were installed immediately downstream. These blocks were replaced by a pair of two-dimensional subsonic contraction blocks with a contraction ratio of 1.5. The contraction contours (cubical arcs) were determined from the data given by Rouse and Hasson (11) on a cavitation prevention basis. The second contraction provided an additional acceleration of the flow to 134 feet per second. It also served the purpose of reducing the nozzle boundary layer thickness.

The compressed air system consists of two high-pressure compressors, air storage tanks, a dryer, and associated valving and piping. One compressor is a two-stage unit, rated at 250 cfm at 600 psig and powered by a 100 h.p. electric motor. The other is a three-stage compressor, rated at 195 cfm at 1500 psig, and driven by a 50 h.p. electric motor. The compressors pressurize a storage volume of 1460 cubic feet to 250 psia (18 atmospheres). The air is dried to a dew point of -40°F prior to storage.

Downstream of the test section the air may be exhausted either to the atmosphere or to multiple vacuum tanks whose total capacity is 22,750 cubic feet. The vacuum system was not used for these studies. Only atmospheric exhaust was employed.

B. The Experimental Model

The test model was mounted two nozzle heights downstream of the nozzle tangency point (see Figure 3). The model consisted of three slats - each 2.1-inches high, 6-inches wide and 0.312-inch thick (see Figures 4 and 5). The slats were mounted in such a way that they resemble the array of ribbons in a ribbon parachute. A single ribbon spacing of 0.537-inch was used. This applies to the two center slots. The outer two slots were 0.337-inch. This value was obtained by selecting a half-slot height plus a nozzle displacement thickness correction. A single geometric porosity (open-to-total area) of 20.5 percent was examined. This porosity was selected since it closely matched the design throat size of the tunnel when operated supersonically; i.e., design subsonic and supersonic mass flows were identical.

At the maximum upstream pressure, the aerodynamic loading was approximately 200 pounds per square inch - or a total loading per slat of approximately one ton. The test slats had to be quite husky to withstand this loading. The three slats were cantilevered from aluminum "windows" on each end as may be observed in Figure 4. Optical windows were embedded in the aluminum windows for shadowgraph/schlieren observations of the slot and shear layer flows. Structural and packaging problems limited the field

Geometric porosity was systematically varied in Reference (2) from 20 percent to 84 percent. Porosity was demonstrated to be an unimportant parameter in determining the heat transfer processes in a subsonic ribbon parachute. This conclusion is undoubtedly still true in supersonic flow as long as the shock remains ahead of the entire parachute entrance.

of view to a 4-inch diameter circle located slightly downstream of the center slat. Two views of the ribbon parachute model, as installed in the wind tunnel, are shown as Figures 4a and 4b. Certain instrumentation details are also visible in these Figures although the reader is referred to Figure 5 for additional construction and instrumentation details.

For structural reasons, only one side of the ribbon was instrumented. The ribbon orientation was fully reversible. The basic structure of the ribbon was a solid bar of type 304 stainless steel. Chambers or compartments were milled in the bar to accept the instrumentation leads and to provide an air gap element of insulation between the forward and rearward-facing surfaces of the ribbons. A removable constant-thickness, stainless-steel, instrumentation-plate was screwed and potted to the main load bearing structure.

Eleven, 36-gauge, calibrated iron-constantan thermocouples were cemented at regular intervals in small holes drilled in the internal face of the instrumentation plate (see Figure 5). A minimum quantity of copper oxide cement was used in the installation. Small rectangular grooves, 0.025-inch deep and 0.040-inch wide, were milled in the stainless steel instrumentation plate. These grooves were filled with Resiweld epoxy cement and the epoxy was shaved flush. Two additional grooves, visible in Figure 4, were provided on the exposed face of the instrumentation plate. These grooves blocked the conductive heat flux by reducing the effective thermal conductivity of the surface material.

Two small tab elements, which covered a portion of the slot region, were brazed to the edge of the main instrumentation plate. The tabs and the main plate were of identical material and of equal thickness. A single

thermocouple was installed in the center of the rear face of each tab. Hollow pressure chambers were soldered to the sheltered face of the instrumentation plate. The pressure taps were drilled (d = 0.020-inch) through the plate into the chambers. A typical pressure tap installation is shown in Figure 5.

III. EXPERIMENTAL STUDIES

A. Uniformity of Approach Flow

As the airflow enters the wind tunnel stagnation chamber, it undergoes a sharp 90 degree turn (see Figures 2 and 3). The perforated plates and the screen were installed to remove any resulting nonuniformities. A 15-tube velocity survey rake, Figure 7, was fabricated to sense the uniformity of the approaching flow velocity. The test ribbon assembly was moved downstream to the last window location. The velocity survey rake was installed in the abandoned test plane. Runs were carried out at upstream pressures of 104 and 74 psia. These pressures exceeded the limits of available manometric instrumentation. A special manometer, visible in Figure 2, was constructed using high pressure, translucent plastic tubing. Water colored with food dye was used as manometer fluid. The specific gravity of this combination, as measured by a hydrometer, was 0.999 at 77°F. A great deal of difficulty was encountered in accurately measuring the differences in impact pressure. For example, at a stagnation pressure of 74 psia, a typical difference in impact pressures was 1/4-inch of water (0.01 psia). The combined effects of high pressure level (74 psia), low pressure difference (0.01 psia), short

This was necessary since the test ribbons provide the choking mechanism required to establish a fixed value of the approach velocity.

wind tunnel running time (30 to 50 seconds), and the various response rates of the individual tubes of the rake, were such that, initially, the manometer board was emptied of fluid on nearly every run. The response problem was examined in bench tests in which the rake-manometer combination was connected to a pressure manifold to which a 100 psia test pressure could be suddenly applied. Satisfactory pressure readings were obtained by measuring the pressure differences between tubes of nearly equal response rates.

The approach flow velocity distribution data are summarized in Figure 8. All velocities are within one percent of the centerline velocity with the exception of the four points taken near the nozzle walls. These latter points all yield low indicated velocities which are undoubtedly due to the nozzle boundary layers. The average approach velocity was found to be 134 feet per second. The uniformity of the approach flow seemed to be within tolerable limits.

B. Ribbon Pressure Ratios

The pressure ratios applied across the ribbon elements are presented in Figures 9 and 10 as a function of the slot sonic Reynolds number Re_{D}^{*} . This quantity is defined as (12)

$$Re_{D}^{*} = \frac{\rho^{*}a^{*}D}{\mu^{*}} = \frac{\rho^{*}}{\rho_{o}} = \frac{\rho^{*}}{\rho_{o}} = \frac{\rho_{o}}{\sqrt{8\pi^{*}}} = \frac{\sqrt{8\pi^{*}}}{\sqrt{8\pi^{*}}} = \frac{\sqrt{8\pi^{*}}}}{\sqrt{8\pi^{*}}} = \frac{\sqrt{8\pi^{*}}}{\sqrt{8\pi^{*}}} = \frac{\sqrt{8\pi^{*}}}{\sqrt{8\pi^{*}}}$$

or

$$Re_{D}^{*} = 5.49 \times 10^{4} P_{1} \text{ (psia)}$$
 (4)

for a stagration temperature of 70°F and a ribbon width of 2.1-inches.

The operating range of the wind tunnel, as determined by a useful running

time of 30 seconds, is P_1 : 20 - 140 psia. Two downstream pressures were measured for reference. The first, P_2 , is the pressure measured at the downstream stagnation point of the ribbon. The second, $P_{\rm exit}$, was measured using a wall static pressure tap installed in the centerline of the last window location (see Figure 3). $P_{\rm exit}$ should correspond to the pressure p measured properly on an actual parachute. This occurs several ribbon widths downstream of a ribbon element.

Since the wind tunnel discharges into the atmosphere, at low flow rates P_{exit} is nearly atmospheric. A sonic or critical pressure ratio is approximately 2. Only the first two points on the left side of Figure 9 are subcritical. All others are supercritical. This point is clear in Figure 10. A comparison of Figures 6, 9, and 10 is quite informative. The critical condition occurs between photo b and photo c of Figure 6. The jets from the two slots diverge as the upstream pressure (and the pressure ratio) is increased. The two diverging jets meet at an Re $_{
m D}^{\infty}$ of approximately 3.5 million. No further jet expansion is possible since the jet flow completely fills the changel downstream of the ribbons. Therefore the pattern becomes stable; i.e., insensitive to further increases in the upstream pressure P_1 . The pressure ratio $P_1/P_{\rm exit}$ remains constant. The ribbon porosity, open-to-total area, is 20.5 percent. This produces a geometric area ratio of 4.88. Expanding onedimensionally, this generates a downstream Mach number of 3.15, and a stagnation-to-static pressure ratio of 46. Actually, the shear layers occupy a portion of the flow area downstream of the ribbons. The measured pressure ratio, P_1/P_{exit} , is 26, which yields an average downatream Bach number of 2.78.

At low Re_D, the discrepancy between P_2 and $P_{\rm exit}$ is a base flow phenomenon. Consider the vertical dashed lines in Figures 9 and 10 at Re_D = 3.3 x 10⁶ (photo c of Figure 6). The jet flow expands to a Mach number of approximately 2.5 and then undergoes a shock recompression* to $P_{\rm exit}$. According to Figure 9, $P_2/P_{\rm exit} = 2.8/12 = 0.23$. The predicted value, according to the base pressure theory of Korst (4), is 0.24.

At large values of Re_D^* , the jets completely fill the duct, the flows are parallel and exhibit the conventional shock diamond pattern. Apparently this pattern continues for some distance down the duct. Beyond $\mathrm{Re}_\mathrm{D}^* = l_{\mathrm{r}} \times 10^6$, P_exit is less than P_2 .

One important conclusion to be drawn from Figure 10 is that the ϕ ribbon pressure ratio is constant at a value of approximately 26 (depending on the definition) for slot sonic Reynolds numbers greater than 4×10^6 . This result applies to the case of atmospheric discharge. In another series of tests, $P_{\rm exit}$ was increased from subatmospheric values to progressively larger values by covering the exhaust flange with stacked layers of perforated plates. In this manner, $P_1/P_{\rm exit}$ was varied from 5 to 26 at a single ${\rm Re}_{\rm D}^*$ of 6.3 x 10^6 . These latter studies will be discussed in Section D.2 (b).

Referring again to Figures 9 and 10, it is necessary to point out that the pressure ratio remains fixed for $\mathrm{Re}_\mathrm{D}^* > h \times 10^6$. Any heat transfer trends which occur at $\mathrm{Re}_\mathrm{D}^* > h \times 10^6$ are truly due to Reynolds number and not due to pressure ratio.

The phenomena observed in Figures 6, 9, and 10 will occur on actual ribbon parachutes. The Reynolds numbers at which the several events would occur are not necessarily related to the present values of Re_{D}^{*} .

The shock is a normal shock in photo c of Figure 6. This quickly reverts to the weak shock system shown in photo f.

C. Ribbon Surface Pressure Distribution

The front surface and rearward surface wall static pressure distributions were obtained using the static pressure taps visible in Figure 5. The results, plotted in Figure 11, present a local pressure at location x divided by the stagnation pressure, at location x=0. It is one-half of the slat height. Notice that the pressures were measured along two vertical lines - alternate points belong to different spanwise stations. The data was taken at small values of x/R in view of the anticipated correlation of results with stagnation flows.

The point x=0 represents the geometric centerline of the ribbon. For supercritical pressure ratios, the pressures along both the front and back surfaces reach maximum values near the geometric centerline. Pressures along the front surface are considerably more uniform than those along the rear surface.

The actual location of the stagnation point was obtained from large scale plots of the pressure distributions. This data is summarized in Figure 12. The apparent stagnation point nearly always fell below the geometric centerline for both the upstream and downstream surfaces. The average displacement (0.06-inch) is not large when one considers the internal diameter of a pressure tap is approximately 0.03-inch. It was not possible to move the apparent stagnation point closer to the geometric

The single exception occurs along the rear face at a subcritical pressure ratio. The application of a stagnation point model to the rear surface does not apply at subcritical pressure ratios.

The ribbons were of finite thickness. The static pressure taps installed in the center of the slot width indicated local Mach numbers well in excess of one. This implies that the sonic line lies near the upstream face of the ribbon. A typical value is $p_{\rm slot}/p_1 = 0.22$ when $P_1 = 165$ psia, $Re_{\rm in}^{\rm X} = 8.5 \times 10^6$.

centerline by a simple rotation of the ribbon. Apparently this slight flow abnormality is a property of the facility.

By assuming that the measured pressures are constant across the thickness of the boundary layer, and that the flow outside of the boundary layer expands isentropically from p_{stag} to p_x , the local velocities just outside of the boundary layer may be determined. This data is presented in Figure 13. Of primary importance in this figure is the fact that both the upstream and downstream velocities grow linearly with distance from the stagnation point. This phenomena is characteristic of stagnation flows and is a familiar result for the upstream surface. Figure 13 presents the strongest evidence for considering the flow adjacent to the downstream surface as a stagnation flow - recalling that this occurs only when supercritical pressure ratios are involved.

Since the velocities outside of the boundary layer grow linearly with distance, the velocity gradient may be computed. These results are presented in Figure 14 * . Two values are given at each $\mathrm{Re}_{\mathrm{D}}^{*}$ for both the forward and rearward surfaces. The asymmetry between the upper and lower values is undoubtedly due to the stagnation point shifts summarized in Figure 12.

The upstream surface velocity gradient is independent of Reynolds number for supercritical pressure ratios. For the fully developed jet flows ($\mathrm{Re}_\mathrm{D}^* \approx 4 \times 10^6$) the downstream surface velocity gradient decreases with Reynolds number. Over the narrow range 3.5 x $10^6 \leqslant \mathrm{Re}_\mathrm{D}^* \leqslant 8.5 \times 10^6$,

$$\sqrt{C} = \sqrt{\frac{dU_8}{dx}} = \text{constant Re}_D^x = \text{constant } (P_2)$$
 (5)

Actually the square root of the velocity gradient is plotted since this quantity is of importance in stagnation point heat transfer calculations.

The measured upstream surface stagnation point velocity gradients may be compared with analytical predictions. For flow over blunt bodies, the first term of the Taylor series expansion for the surface velocity is the linear relation

$$U_{8} = Cx, \qquad (6)$$

where C is the local velocity gradient-external to the boundary layer. For reference, the stagnation point velocity gradient is expressed by

$$C = \frac{\beta \ U_{\infty}}{R} \tag{7}$$

where U_{co} is the subsonic velocity approaching the body and R is the body radius. β is a constant depending on body geometry. The following table illustrates a few numerical values of β .

Geometry	$\underline{\beta}$	Reference
Circular Cylinder	2	13
Sphere	3/2	13

Using an approach velocity of 134 feet per second, a body radius of $\frac{1.05}{12}$ feet, and a β of 2 yields

$$\sqrt{C} = \sqrt{\frac{\beta U_{co}}{R}} = \sqrt{\frac{(2)(134)}{\frac{1.05}{12}}} = 55 \text{ sec}^{-1/2},$$

a value which is 24 percent larger than the measured value.

Methods for predicting the maximum recirculation zone velocity (U_b for the rear face) are being developed. For the present experimental conditions, reference (7) gives

$$2\left(\frac{u_{b}}{v_{j}}\right)\left(\frac{\rho_{b}}{\rho_{j}}\right)\sigma\tan\alpha = \frac{1}{2} \tag{8}$$

where

- is the mean recirculation velocity
- is the mean jet velocity downstream of the slot at the maximum jet width = 2000 ft/sec
- is the mean recirculation zone density, $\text{is the mean jet density corresponding to } U_j, \frac{\rho_j}{\rho_b} = \frac{T_b}{T_j} = \underbrace{\frac{T_b}{T_{0,j}}}_{\approx 1} \cdot \underbrace{\frac{T_{0,j}}{T_{j,j}}}_{f(M_j)}$
- ing the jet mixing layer spreading factor, 20
- is the jet expansion half-angle, $\tan \alpha = 0.2$

Substituting these values into Equation 3.6 yields

$$U_{l_3} = 280 \text{ feet per second}$$

$$\sqrt{G} = \sqrt{\frac{(2)(280)}{1.05}} = 81 \text{ sec}^{-1/2}.$$

- D. Heat Transfer Measurements
- Forward Facing Surface 1.
 - (a) Recovery Temperature Distribution

The 30-50 second wind tunnel running time did not permit a standard "run-to-recovery" which normally requires 30 to his minutes. Extrapolation techniques had to be adopted. Two tunnel runs were made to find the one thermocouple of the seven installed in the stagnation temporature rake which responded closest to the average of the seven. Four runs were then made to determine the distribution of recovery temperatures. For these runs the model was allowed to respond thermally and to approach the adjubatic condition. The indicated model temperatures $\mathrm{T_i}$ and tunnel total temperatures $\mathrm{T_o}$ were measured as a function of time. The extrapolations to zero heat transfer were made by plotting $\mathrm{T_i/T_o}$ versus 1/1 and examining the curve for the limit as r increases. The extrapolations never involved a temperature change of more than 2°F from the last measured value. The upstream surface recovery temperature ratios are given in Figure 15. At the stagnation point, x/R = 0, the recovery temperature should equal the freestream total temperature at these low temperature levels. This is not always the case (see Figure 15, x/R = 0), a phenomena undoubtedly due to thermal conduction in the surface of the model. A one percent change in T_i/T_o corresponds to a 5.4 degree Fahrenheit change in the indicated recovery temperature. The relatively low recovery temperatures in the slot reflect the large velocities that exist there. It is important to note that the equilibrium temperatures in the slot are lower than at the stagnation point. The steady state operational temperature of a parachute is determined by the conditions at the stagnation point and not at the slot*.

(b) Heat Transfer Runs

The general heat transfer experimental technique is described in detail in Appendix A. The technique consisted of precooling the model by packing dry ice around the ribbons and waiting for 10 to 15 minutes until the surface temperature was $-108 \stackrel{4}{-} 1^{\circ} F$. The tunnel was started rapidly

In Section 2, the discussion of Figure 28 points out that the heat transfer coefficients in the slot are 6 or 7 times those at the stagnation point. Therefore, transfer operational temperatures are determined by conditions in the slot.

(in less than 1 second after the initiation of the valve actuator*). The dry ice was blasted off by the air stream. The model heated up under the direct action of both forced convection and the heat capacity of the instrumented skin of the model. Heat transfer coefficients were calculated for several times using Equation A-14 of Appendix A. The heat transfer coefficients were extrapolated to zero time (a uniform wall temperature condition) ignoring data taken in the first 1-1/2 seconds. Model thermal symmetry was verified such that only one-half of the central ribbon was extensively studied. The stagnation point shifts, observed by means of the surface pressure distributions, were also clear in temperature distribution plots made at several time conditions. The reader is again referred to Appendix A where a sample run is illustrated and the various steps in the data reduction process are illustrated.

The dimensional upstream stagnation point heat transfer coefficients are presented in Figure 16. The data was taken for Reynolds numbers as high as ten times those previously obtained (10^{7}). The heat transfer coefficients increase with nearly the one-half power of the Reynolds number, a situation typical of laminar stagnation point boundary layers. The scatter in the data is approximately $\frac{1}{2}$ 10 percent. The heat transfer and

During the period after the upstream plug valve begins to open, there is a rapid compression of the air in the stagnation chamber which lasts about I second. The indicated stagnation temperature, as indicated by seven shielded 36-gauge iron-constantan thermocouples, rises sharply. After an indicated temperature rise of nearly 500F, the temperature dropped to within a few degrees of room temperature and then decreased at a rate depending on the rate that mass was removed from the storage tanks. The initial transients (valve opening time, compression in the stagnation chamber, downstream pressure decrease to the desired subatmospheric level) were clearly visible in the data transes and were completed in 1-12 seconds (with the exception of the aforementioned stagnation temperature drop).

and pressure data at the upstream stagnation point are combined in a dimensionless group in Figure 17. The parameter

$$\frac{\text{Nu}_{\mathbf{w}}}{\sqrt{\text{Re}_{\mathbf{w}}}} = \frac{\frac{h\mathbf{x}}{\mathbf{k}_{\mathbf{w}}}}{\sqrt{\frac{\rho_{\mathbf{w}}U\mathbf{x}}{\mu_{\mathbf{w}}}}} = \frac{\frac{h}{\mathbf{k}_{\mathbf{w}}}}{\sqrt{\frac{\rho_{\mathbf{w}}}{\mu_{\mathbf{w}}}C}} \tag{9}$$

is equal to 0.49 (13) for a laminar two-dimensional, stagnation point for a wall-to-stream temperature ratio of 0.7. Since the data was extrapolated to time $\tau=0$, the dry ice temperature was used in evaluating the gas properties k_w , δ_w , and μ_w . The density and velocity gradients were obtained from the pressure measurements, Figures 9 and 14, respectively.

The data agrees with stagnation point predictions for low Reynolds numbers (1 x $10^6 \le \text{Re}_D^* \le \text{r}$ x 10^6). At higher Reynolds numbers the data falls 20-30 percent above the two-dimensional laminar stagnation point boundary layer analysis of Reshotko and Cohen (13). The applied pressure ratio increases with Re_D^* in Figure 17. The flagged points in Figure 17 represent data taken at $\text{Re}_D^* = 6.3 \times 10^6$ at several applied pressure ratios (also see Figure 27). As mentioned in Figure 3, for these tests with increased downstream pressure, a stacked set of perforated plates covered the exhaust opening. The downstream pressure, p_{exit} , was varied by changing the overlay of the perforated plates. The flagged points represent forward surface heat transfer measurements taken over a range of p_1/p_{exit} of 5 to 25.

The local distribution of heat transfer coefficients on the upstream side is presented in Figure 18. For easy reference, the local values were non-dimensionalized using the stagnation point values given in Figure 16. This was done in view of the overall aim of correlating all results with the stagnation point heat transfer which may be predicted with precision.

The data of Figure 18 has been corrected for stagnation point shift such that x represents the actual distance from the stagnation point and R, the distance from the true stagnation point to the slot. Some typical faired curves demonstrate that the local distributions are not universal but are strongly dependent on Reynolds number. Local heat transfer increases rapidly away from the stagnation point. Local heat transfer coefficients were observed which were eight times the stagnation point value. Further attempts to correlate local heat transfer coefficients with stagnation point values were abandoned at this point because of the uncertainties involved in the distributions. The curve labeled $\operatorname{Re}_{D}^{*}=0.99$ x 10^{6} in Figure 18 represents a subcritical pressure ratio. This distribution agrees well with comparable subcritical measurements reported in reference (2). Higher Reynolds number distributions generally yield higher local values relative to the stagnation point level.

The average upstream surface heat transfer coefficients are presented in Figure 19. This data was obtained by numerical integration of the local distributions illustrated in Figure 18. Notice that the average heat transfer coefficients increase linearly with Reynolds number. This is to be compared with the normal laminar square root dependence.

In Figure 20, the average Nussell numbers, defined as

$$Nu_{avg} = \frac{h_{avg}D}{k_0}$$
 (10)

are plotted for the upstream side. The characteristic length in both Nussell and Reynolds numbers is the width of the ribbon. The characteristic velocity in the Reynolds number is the velocity in the slot. This enables a comparison of present heat transfer data with previous ribbon

parachute data (2) and data obtained on tube banks where it is customary to base the Reynolds number on the tube diameter and on the velocity in the narrowest cross section ($\Omega_{\rm b}$).

The subcritical data of Reference (2) is presented in Figure 20 to illustrate the overall Reynolds number dependence. The increase of the slope of the curve with higher Reynolds numbers, first observed here in Figure 17, has been observed by other investigators on circular cylinders and tube bundles (14, 15).

2. Rearward Facing Surface

(a) Recovery Temperature Distribution

The recovery temperature data is summarized in Figure 21. The sharp rise in recovery temperature at $\text{Re}_D^* \approx 2.5 \times 10^6$ may be correlated with the establishment of a completely supersonic jet flow downstream of the slots (see Figure 6). The primary variation of the recovery temperature ratio, T_{aw}/T_0 is with pressure ratio and not Reynolds number. For $\text{Re}_D^* \approx 1 \times 10^6$ the constancy of T_{aw}/T_0 reflects the constancy of pressure ratio (see Figure 10).

The solid symbols in Figure 20 represent data taken in two different test facilities and using different experimental techniques. The agreement between the three experiments is reassuring.

At low subsonic Reynolds numbers a vortex system is formed in the wakes behind obstacles. The phenomena is characterized by periodic vortex shedding. A suppression of the vortex sheet has been accomplished by a splitter plate which increases the Lemperature recovery factor $r: (T_{aw} - T_{\delta})/(T_{o} - T_{\delta})$ from 0.1 to 0.8-0.9 (16). At transonic and

supersonic speeds where the vortex sheet disappears, the recovery factors are again 0.8-0.9. Shadowgraph observations of the supersonic case reveal a stable vortex pattern with no shedding. The expansion-shock pattern stabilizes the flow pattern according to the laws of forbidden signals.

(b) Heat Transfer Runs

The heat transfer coefficients measured at the downstream stagnation point are presented in Figure 22. A comparison of Figures 16 and 22 reveals that the downstream stagnation point heat transfer rates exceed the upstream stagnation point values for $\mathrm{Re}_\mathrm{D}^{\pi} < 6 \times 10^6$. This is rather surprising when one considers the downstream density is considerably smaller. The initial decrease in $h_{\rm stag}$ with $Re_{\rm D}^{\times}$ is probably due to the density decrease (Figure 9). The sharp rise in the range 2 x $10^6 \le \mathrm{Re}_\mathrm{D}^* \le 6 \times 10^6$ might possibly result from the increased recirculation velocities (7). The fraction of the shear layer flow which is reversed decreases slightly as the pressure ratio (and the jet Mach number) is increased. Since the density in the recirculation zone decreases, increased recirculation zone velocities are required. Equation 3.5 relates a stagmation point velocity gradient to an approach velocity. On the other hand, the velocity gradient measurements on the rearward facing surface (see Figure 14) exhibit a decrease in magnitude as Re_D is increased. Therefore, both the density and the velocity gradient are decreasing with increasing $\mathrm{Re}_\mathrm{D}^{\#}$ while the heat transfer coefficient is increasing. These behavior patterns are not typical of ordinary stagnation flows.

The apparently sharp discontinuity in the results at $\mathrm{Re}_\mathrm{D}^{\%} \approx$ 6×10^6 is not understood at the present time. No discontinuous process is observable in any of the photographs or graphs at this point. The downstream stagnation point heat transfer data are compared with two-dimensional laminar stagnation point analyses in Figure 23. The velocity gradient and density were obtained from Figures 9 and 14. Additional experimental results are presented for the condition of elevated exhaust

pressures. The results are not in complete agreement; either with each other or with laminar stagnation point analysis. A few of the points compare well with analysis while the rest do not. Two possible explanations are the increased turbulence level of the recirculating flow at high ${\rm Re}_{\rm D}^{\, \alpha}$ and/or that the recirculating flow pulsates between several patterns.

The distributions of heat transfer coefficients on the downstream side are given in Figure 24. The average or integrated values are presented in Figure 25. The combination of effects produce an average heat transfer coefficient which is independent of Reynolds number. The abnormalities in the stagnation point heat transfer variations with $\text{Re}_D^{\#}$ are masked. This fact, coupled with the complex distributions given in Figure 214, make it difficult to compare the behavior of the average and stagnation point heat transfer coefficients. A comparison of Figures 19 and 25 reveals that the downstream average heat transfer coefficients fall well below the corresponding upstream average values. This point is pursued in Figu. 26. Faired curves through the upstream and downstream average heat transfer coefficients are given over a wide Reynolds number range. At low Reynolds numbers the head transfer on the front side is greater than that on the back side. With increasing Reynolds number the heat flux to the back side increases more rapidly and for $Re_D^* = 50,000$ it is as high as on the front side - and even higher as $\mathrm{Re}_\mathrm{D}^{*}$ is increased further. This is a behavior pattern which agrees quantitatively with tubes and tube bundles in cross flow (16).

The present data continue the trends described above for subscritical pressure ratios. However, for critical pressure ratios, the downstream heat transfer becomes progressively less than the upstream. If the stagnation point analogy is valid, the ratio of upstream to downstream

The pressure ratios for the two lowest Reynolds number points of the present experiment are subcritical.

average heat transfer flux should vary directly with the square root of the density ratio or approximately with $(p_1/p_2)^{1/2}$. As an example choose $\text{Re}_0^2 = 8 \times 10^6$. From Figure 10, $(p_1/p_2)^{1/2} \approx 5$. From Figures 19 and 25, $h_{up}/h_{down} = 375/120 \approx 3$. Thus the proper pressure ratio trend is observed.

The problems are not completely understood, however. A summary of data taken at $\mathrm{Re}_\mathrm{D}^\mathrm{x}=6.3\,\mathrm{x}\,10^6$, with several exit pressures, is given in Figure 27. The upstream pressure is held constant in this figure while the downstream pressure is varied. The pressure ratios are all supercritical. The upstream heat transfer is sensibly independent of the downstream exit pressure. However, the downstream stagnation point heat transfer coefficient decreases as the exit pressure is increased. From Figure 10 it can be concluded that the variations in $\mathrm{P}_{\mathrm{exit}}$ did not affect P_2 .

The final figure, Figure 28, presents measurements of the slot heat transfer coefficient taken with the instrumented surface facing forward (bottom slot) and rearward (after rotation on the top slot).

The data displays the slight asymmetry found in all measurements and points out that the extreme heat flux rates occur in the slot.

Undoubtedly the slot heating rates depend on the ribbon thickness or thickness ratio. Figures 15 and 28 summarize the slot heat transfer behavior as follows: (1) the heat transfer coefficients in the slot are the largest observed on the ribbon; and, (2) the equilibrium temperatures in the slot are the lowest observed on the ribbon. Slot heat transfer is of major importance in transient problems.

IV. CONCLUSIONS

Experiments have been performed on models representing the individual ribbons of a ribbon parachute. The recovery factor and heat transfer coefficient results obtained are valid in the continuum flow regime at franktl number values of approximately 0.7. These results extend the region of available experimental heat transfer data on ribbon parachutes to include ${\rm Re}_{\rm B}^{**}$ of 3,000 to 10,000,000. The average measured Nusselt numbers are presented in Figure 26. It was found that the maximum local heat transfer coefficient exists at the edges of the ribbon. Also the maximum local values on both the upstream and downstream sides also occurred at the edges. The central regions of the upstream and downstream sides exhibited behavior similar to lominar stagnation point boundary layers. The relative minimum heat flux rates occurred at the stagnation point for each surface-flow orientation. Attempts to correlate the gross ribbon heat transfer characteristics with the upstream stagnation point heat transfer predictions were only partially successful.

Large differences in local heat transfer behavior were attributable to the onset of some flow in the slots between the ribbons. The applied pressure ratio was demonstrated to affect the ratio of average upstream to average downstream heat transfer coefficients.

REFERENCES

 Chernowitz, G., and DeWeese, J.H.: "Performance and Design Criteria for Deployable Aerodynamic Decelerators," Air Force Flight Dynamics Laboratory, Wright-Patterson Air Force Base, Ohio, ASD-TR-61-579, December 1963.

- 2. Schoeck, P.A., Hool, J.N., and Eckert, E.R.G.: "Experimental Studies for Determining Heat Transfer on the Ribbons of Fist Type Parachutes," University of Minnesota, Heat Transfer Laboratory Technical Report No. 24, September 1959.
- 3. Koh, J.C.Y., and Hartnett, J.P.: "Measured Pressure Distribution and Local Heat Transfer Rates for Flow Over Concave Hemispheres," Presented at the Semi-Annual Meeting of the American Rocket Society, Los Angeles, Calif., May 9-12, 1960.
- 4. Korst, H.H., Chow, W.L., and Zumwalt, G.W.: "Research on Transonic and Supersonic Flow of a Real Fluid at Abrupt Increases in Cross Section (Final Report)," University of Illinois Engineering Experiment Station Technical Report 392-5, December 1959.
- 5. Chapman, D.R.: "A Theoretical Analysis of Heat Transfer in Regions of Separated Flow," NACA TN 3792, October 1956.
- 6. Larson, R.E., Scott, C.J., Elgin, D.R., and Sciver, R.E.: "Turbulent Base Flow Investigations at Mach Number 3," University of Minnesota Rosemount Aeronautical Laboratories' Research Report 183, July 1962.
- 7. Scott, C.J.: "The Influence on Turbulent Base Pressure and Heat Transfer of Distributed Mass Addition Into the Near-Wake Region of a Supersonic Body of Revolution," Ph.D. Thesis, University of Minnesota, Department of Mechanical Engineering, August 1964.
- 8. Sogin, H.H., Burkhard, K., and Richardson, P.D.: "Heat Transfer in Separated Flows, Parts I and II," Brown University, Aeronautical Research Laboratory, Wright-Patterson Air Force Base, Ohio, ARL 4, January 1961.
- 9. Domich, E.G., Jantscher, H.N., and Olson, D.N.: "Aeronautical Research Facilities," University of Minnesota Rosemount Aeronautical Laboratories Research Report No. 152, September 1958.
- 10. Baines, W. D., and Peterson, E.G." "An Investigation of Flow Through Screens," Iowa Institute of Hydraulic Research Report No. 2, July 1949.
- Rouse, H., and Hasson, M.M.: "Cavitation—Free Inlets and Contractions," Mechanical Engineering, March 1949.
- 12. NACA Ames Research Staff: "Equations, Tables, and Charts for Compressible Flow," NACA TR 1135, 1953.

REFERENCES (cont'd)

- 13. Reshotko, M., and Cohen, C.B.: "Heat Transfer at the Forward Stagnation Point of Blunt Bodies," NACA TN 3513, 1955.
- 14. Grimison, E.D.: Transactions of the American Society of Mechanical Engineers, Vol. 59, pp 583-594, 1937.
- 15. Hilpert, R.: "Waermeabgabe von geheizten Drachten und Rohren im Luftstrom," Forsch. Gebiete Ingenieurw, 4:215, 1933.
- 16. Thomann, H.: "Measurement of the Recovery Temperature in the Wake of a Cylinder and of a Wedge at Mach Numbers Between 0.5 and 3," Report 84, FFA, Stockholm, AD 22 8 867, 1959.
- 17. Eckert, E.R.G.: <u>Introduction to the Transfer of Heat and Mass</u>, McGraw-Hill Book Company, Inc., New York, 1950.
- 18. Gubareff, G.G., and Ko, Shao-Yen: "Review of the Thermal Radiation Property Values of Metals and Other Materials," Minneapolis Honeywell Research Center Report GR 2462-R3, May 1956.

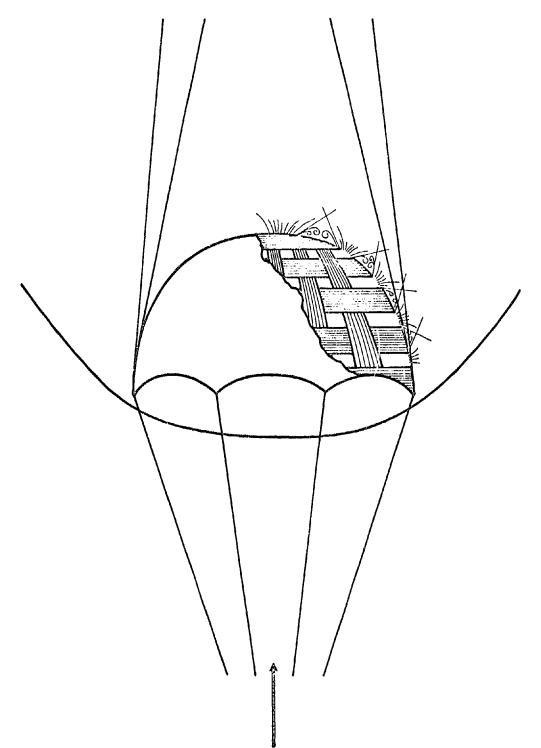


FIGURE 1. SKETCH OF RIBBON PARACHUTE FLOW PATTERNS

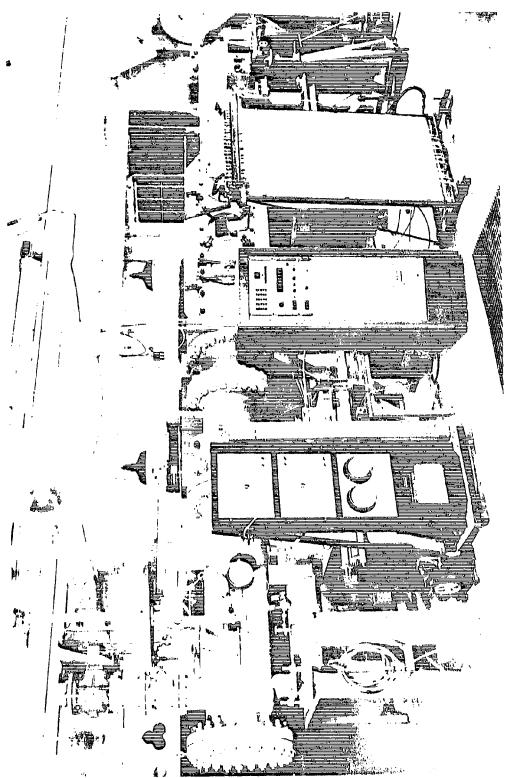


FIGURE 2. PHOTOGRAPH OF THE EXPERIMENTAL APPARATUS SHOWING THE PRESSURIZED SUBSONIC WIND TUNNEL

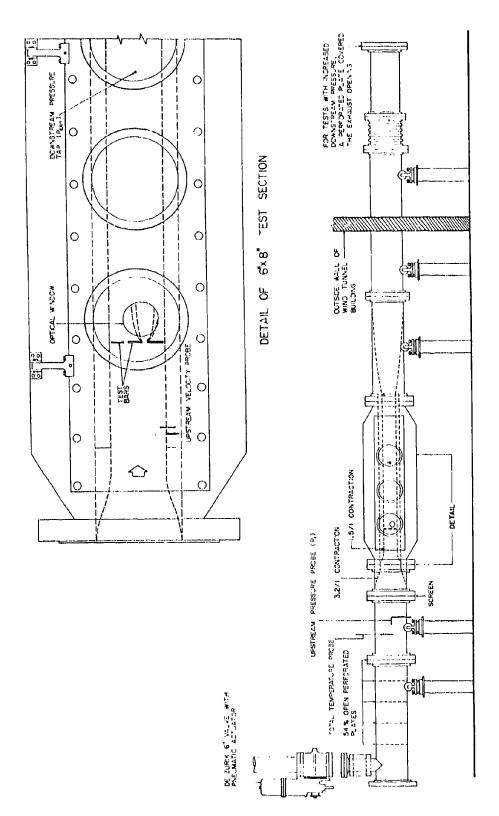
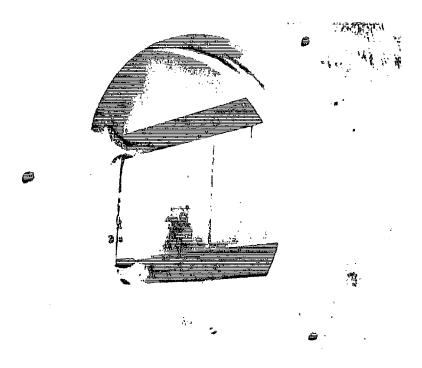
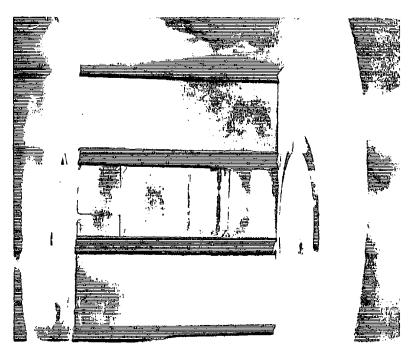


FIGURE 3. SKETCH OF THE TEST SECTION OF THE PRESSURIZED SUBSONIC WIND TUNNEL

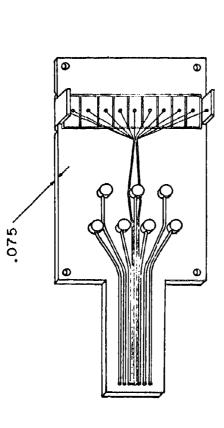


(a) SIDE VIEW THROUGH WINDOW



(b) REAR VIEW LOOKING UPSTREAM

FIGURE 4. RIBBON PARACHUTE MODEL INSTALLED IN THE WIND TUNNEL



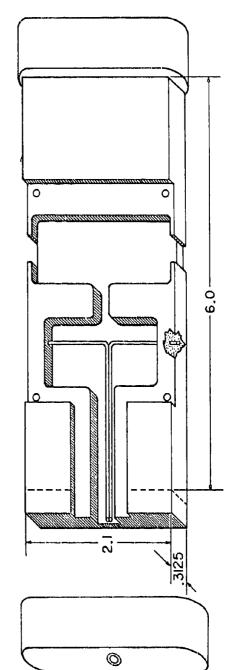
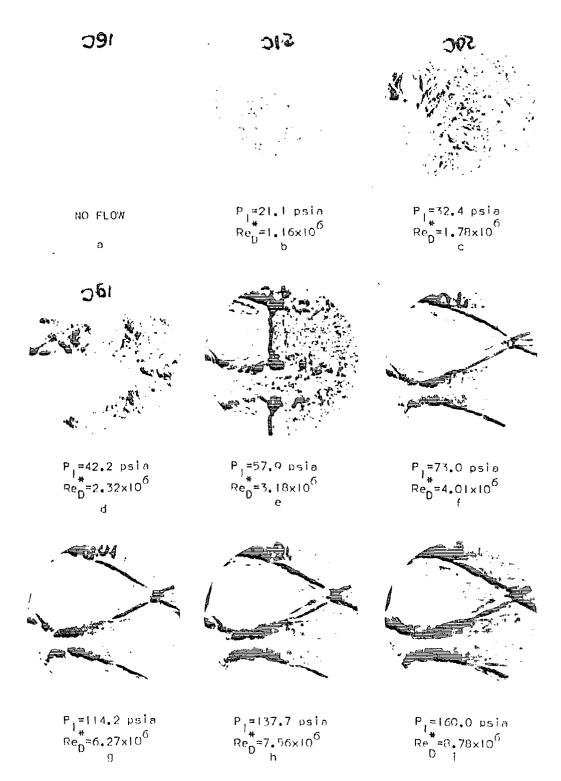


FIGURE 5. SKETCH OF RIBBON PARACHUTE MODEL SHOWING CONSTRUCTION AND INSTRUMENTATION DETAILS



II VANGERISH BITARI KARIMATIKAN BARIMATIKAN BARIMATIKAN MATALIKAN BARIMATIKAN BARIMATIKAN MATALIKAN BARIMATIKAN

FIGURE 6. SHADOWGRAPH PHOTOGRAPHS OF THE FLOW DOWNSTREAM OF THE SLOTS



FISUPE 7. APPROACH FLOW VELOCITY DISTRIBUTION RAKE

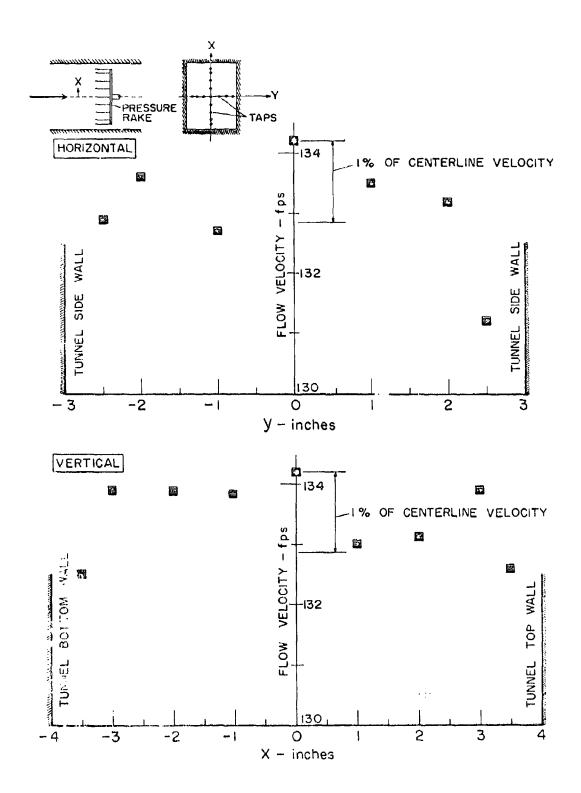


FIGURE 8. UNIFORMITY OF APPROACH FLOW VELOCITIES

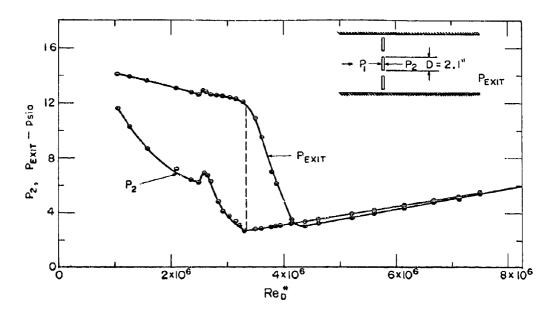


FIGURE 9. VARIATION OF DOWNSTREAM PRESSURES WITH RIBBON REYNOLDS NUMBER

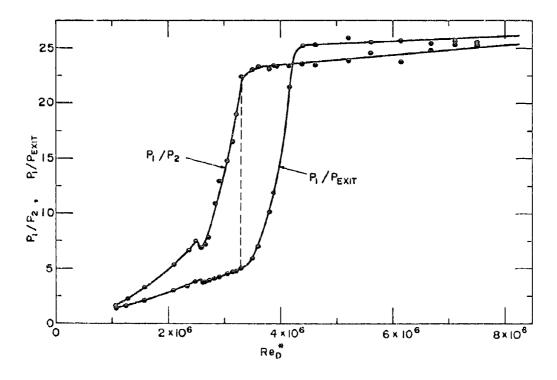


FIGURE 10. PRESSURE RATIOS ACROSS THE RIBBON VERSUS RIBBON REYNOLDS NUMBER

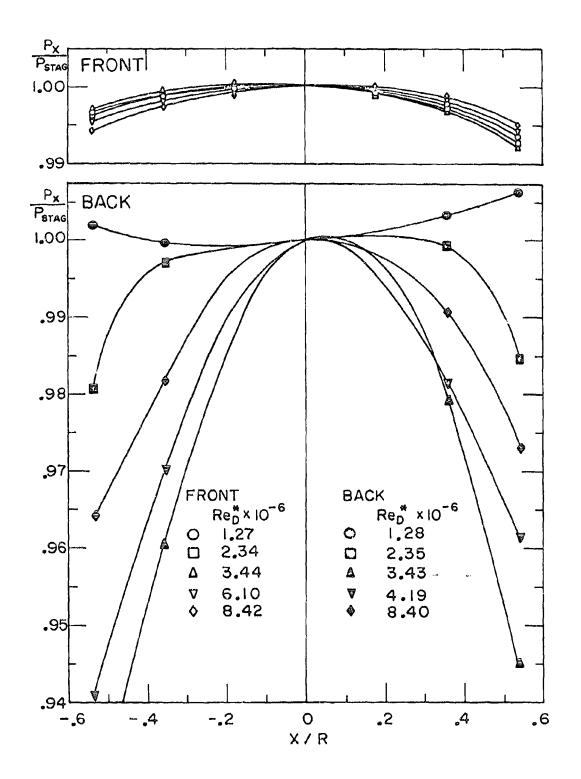


FIGURE 11. TYPICAL SURFACE PRESSURE DISTRIBUTIONS ON THE CENTER RIBBON

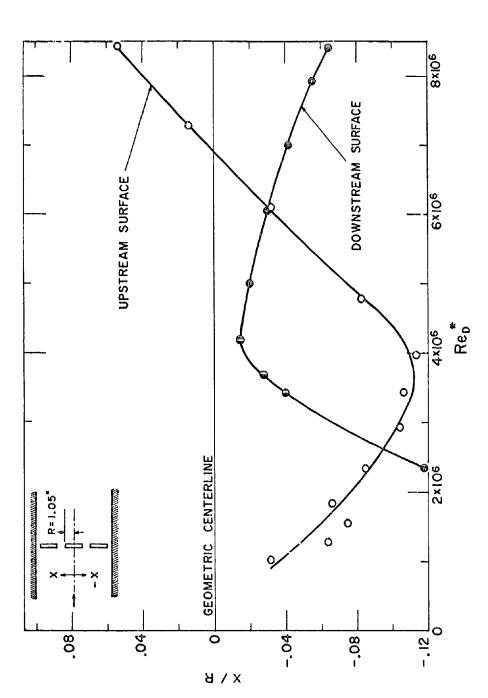


FIGURE 12. THE SHIFT IN THE STAGNATION POINT LOCATION AS INDICATED BY SURFACE PRESSURE MEASUREMENTS

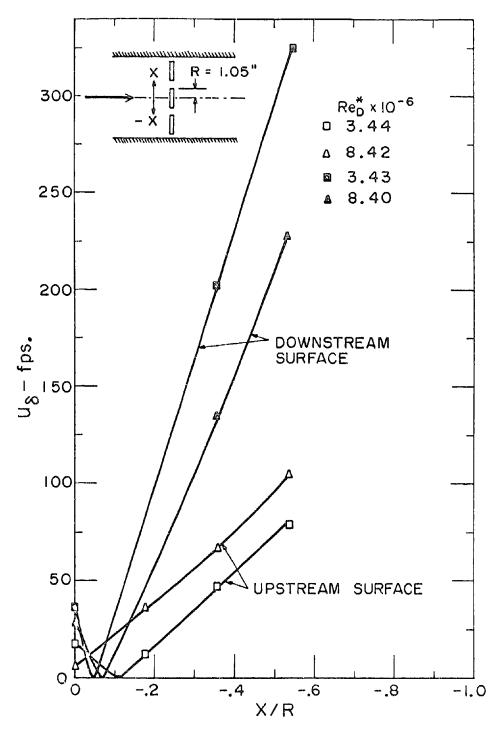


FIGURE 13. RIBBON SURFACE VELOCITY DISTRIBUTIONS

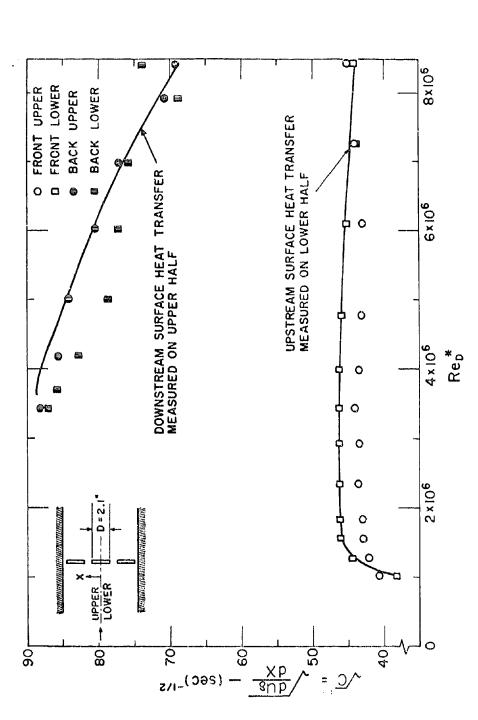


FIGURE 14. STAGNATION POINT VELOCITY GRADIENTS CALCULATED FROM SURFACE STATIC PRESSURE MEASUREMENTS

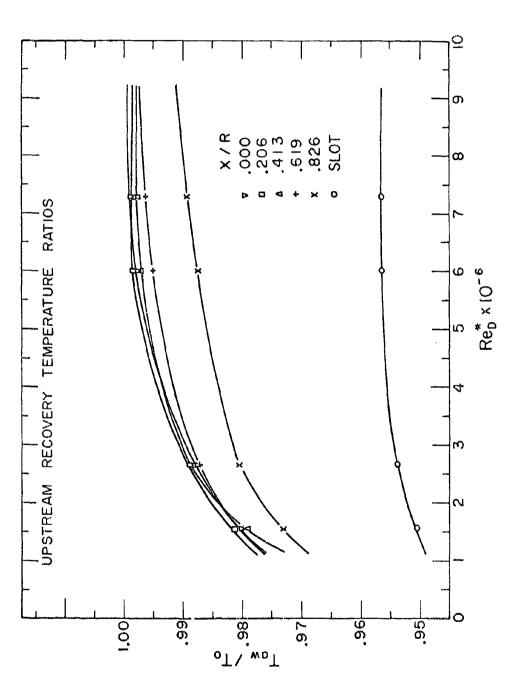


FIGURE 15. RECOVERY TEMPERATURE RATIOS FOR THE UPSTREAM SIDE

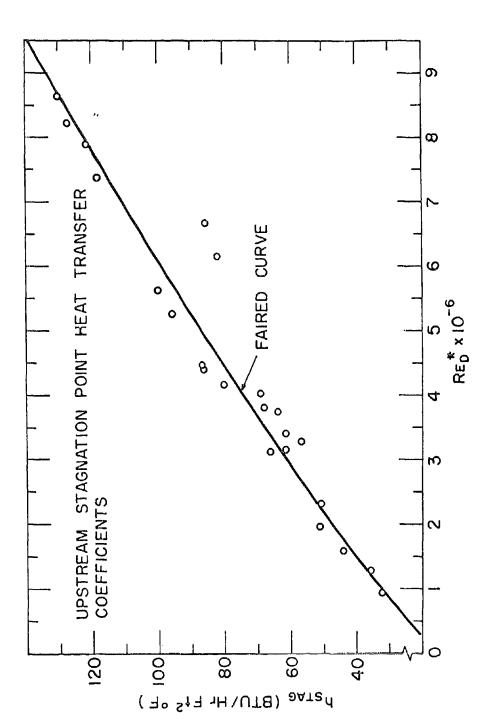


FIGURE 16. UPSTREAM STAGMATION POINT HEAT TRANSFER COEFFICIENTS

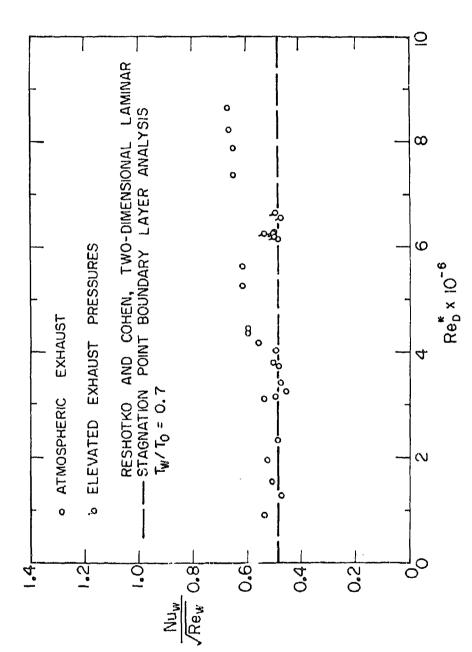


FIGURE 17. CORPELATION OF UPSTREAM STAGNATION POINT HEAT TRANSFER AND PRESSURE DATA WITH LAMINAR STAGNATION POINT BCUNDARY LAYER ANALYSIS

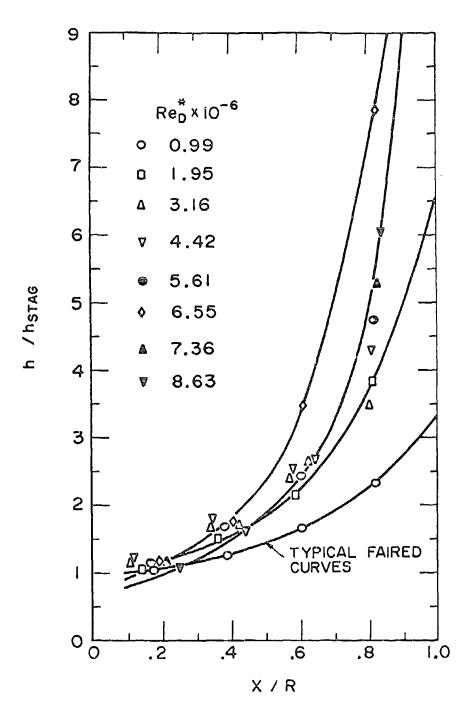


FIGURE 18. DISTRIBUTION OF HEAT TRANSFER COEFFICIENTS ON THE UPSTREAM SIDE

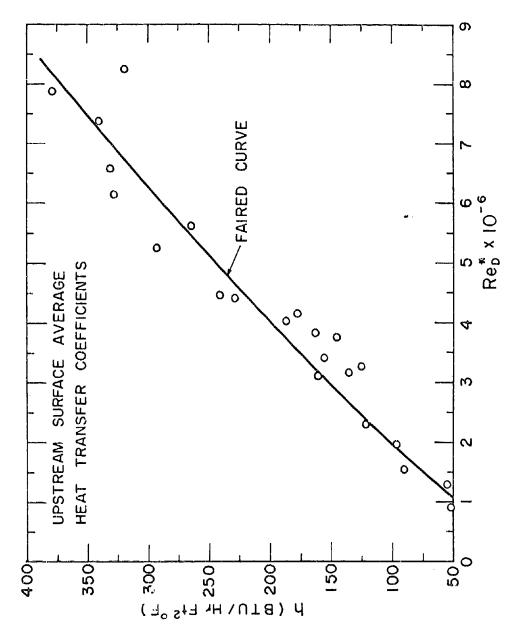


FIGURE 19. AVERAGE HEAT TRANSFER CCEFFICIENTS ON THE UPSTREAT SIDE

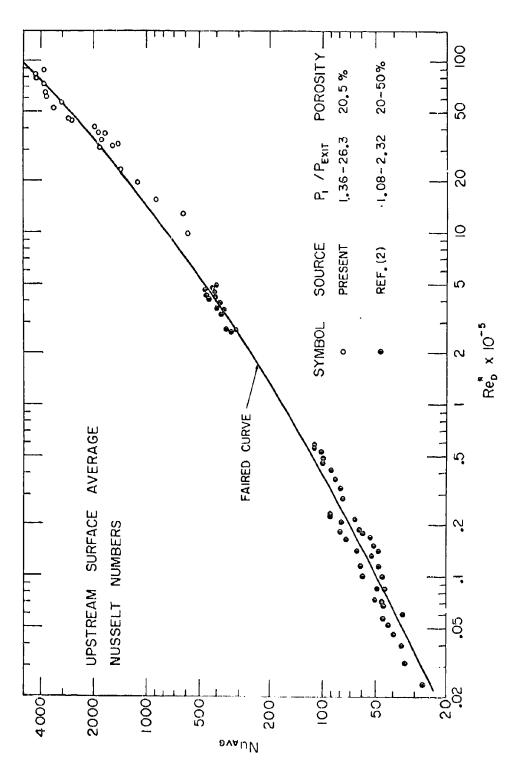


FIGURE 20. COMPARISON OF PRESENT RESULTS WITH PREVIOUS EXPERIMENTS ON RIBBON PARACHUTE HEAT TRANSFER

oborstan vormerandalmennin delimbiren purkunkan men urungki indiliki brilimkilardi. Kalin esti esti esti esti e

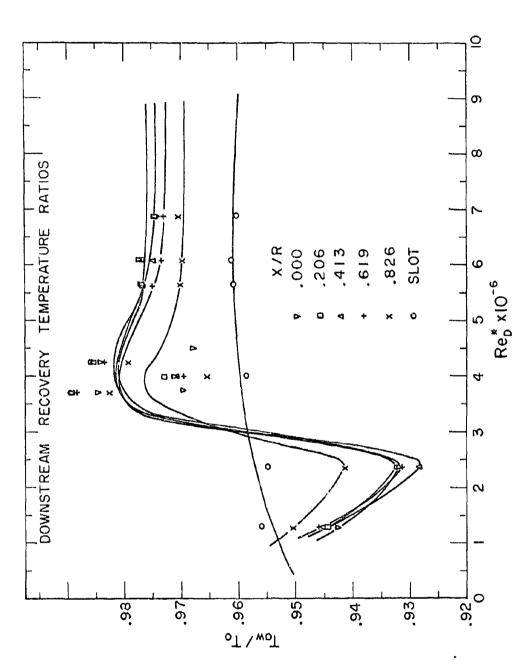


FIGURE 21. RECOVERY TEMPERATURE RATIOS FOR THE DOWNSTREAM SIDE

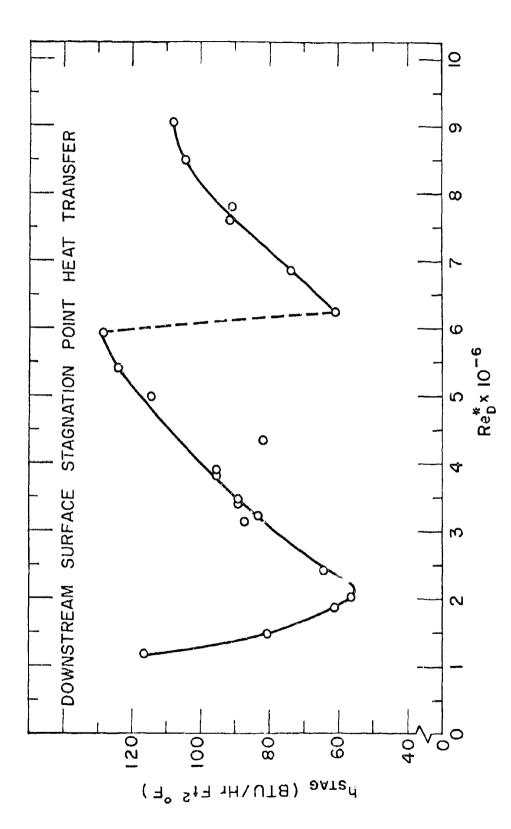


FIGURE 22. DOWNSTREAM STAGMATION POINT HEAT TRANSFER COEFFICIENTS

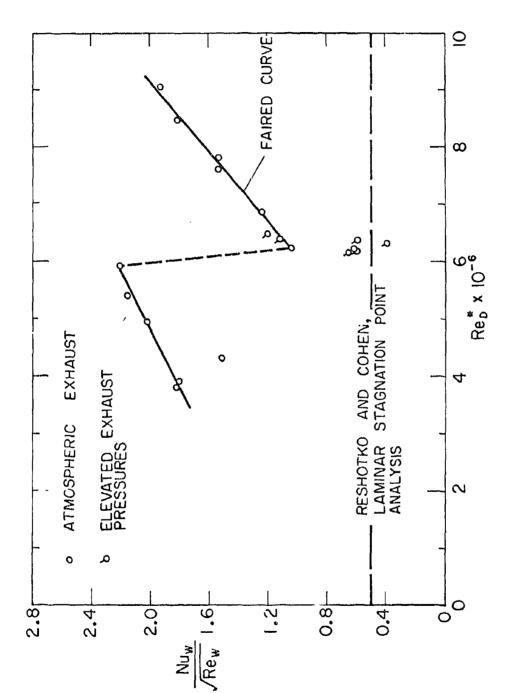


FIGURE 23. CORRELATION OF DOWNSTREAM STAGNATION POINT HEAT TRANSFER AND PRESSURE DATA WITH LAMINAR STAGNATION POINT BOUNDARY LAYER ANALYSIS

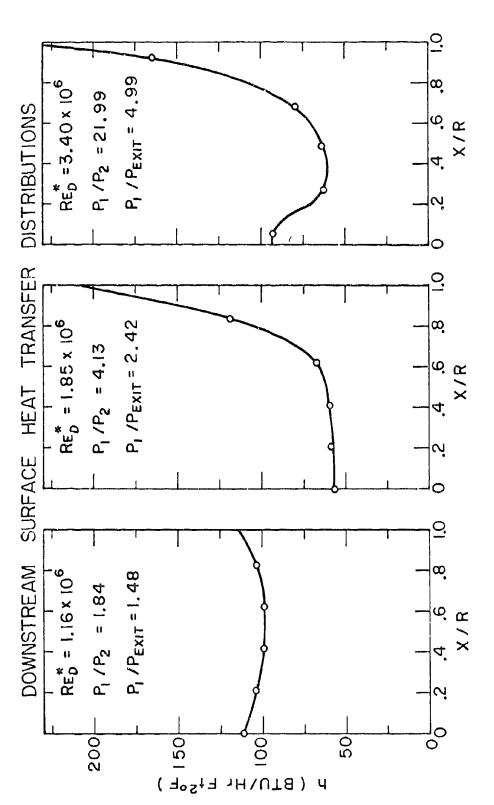


FIGURE 24. DISTRIBUTION OF HEAT TRANSFER COEFFICIENTS ON THE DOWNSTREAM SIDE

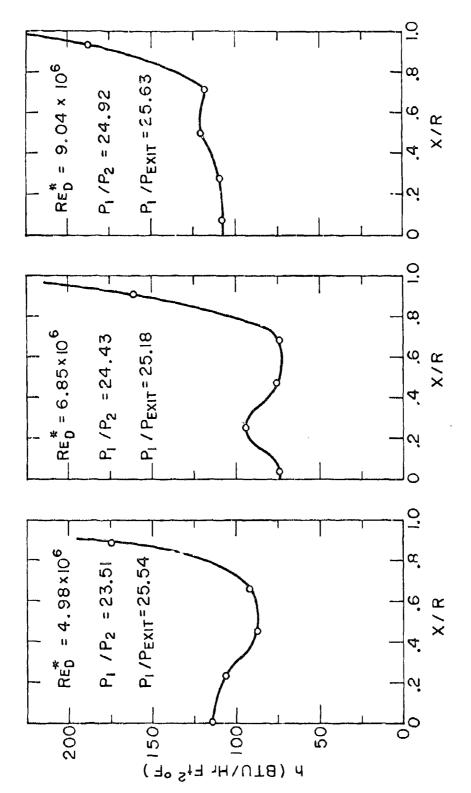


FIGURE 24. Continued

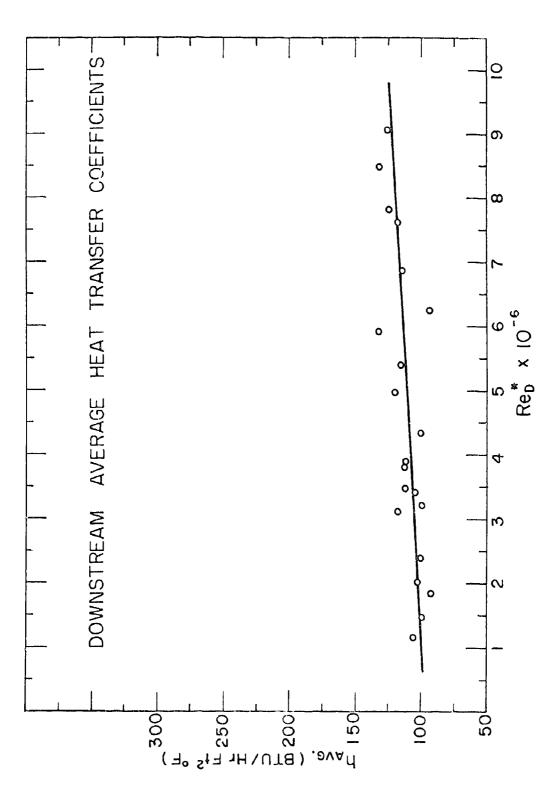


FIGURE 25. AVERAGE HEAT TRANSFER COEFFICIENTS ON THE DOWNSTREAM SIDE

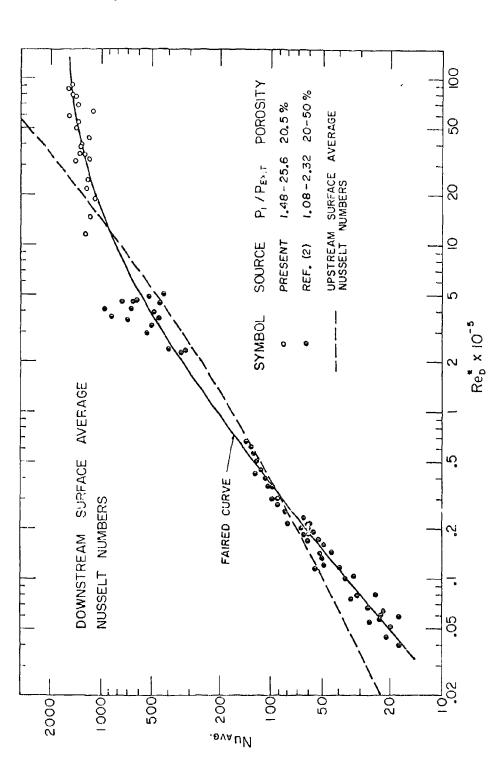
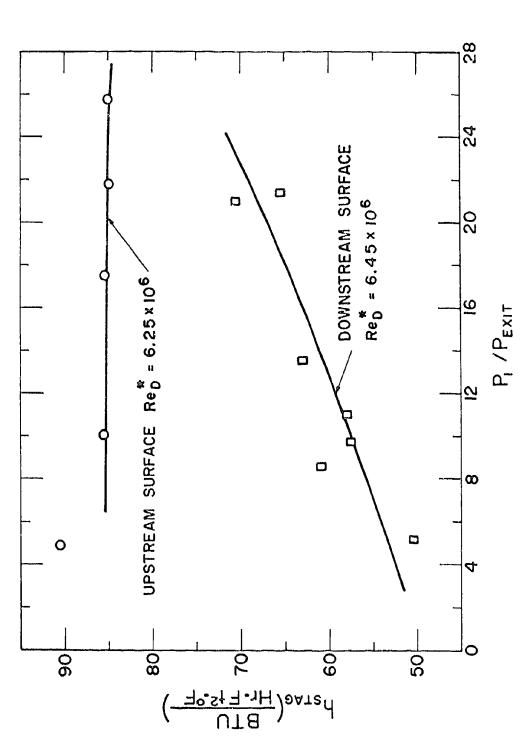


FIGURE 26. COMPANISON OF PRESENT RESULTS WITH PREVIOUS EXPERIMENTS ON RIBBON TARACHUTE HEAT TRANSFER



VARIATION OF BOTH UPSTREAM AND DOWNSTREAM STAGMATION POINT HEAT TRANSFER RATES WITH THE PRESSURE RATIO ACROSS THE RIBBON FIGURE 27.

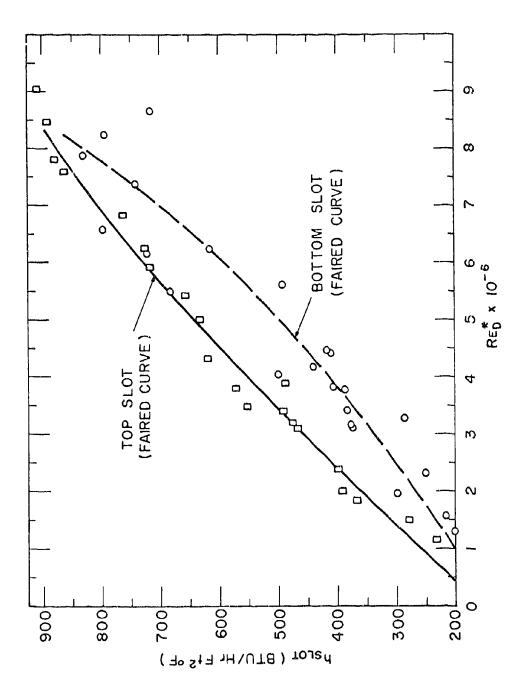


FIGURE 28. HEAT TRANSFER DATA AT THE CENTER OF THE SLOT OF A RIBBON PARACHUTE OF EXASCERATED THICKNESS

APPENDIX A

1. Transient Energy Balance

The transient technique relies on the heat capacity of the model skin for the experimental determination of convective heat flux. The general heat balance on a small element of surface must include

q _{bl} - the heat flux to/from the boundary layer	term I
q _{st} - the heat stored	II
q _{cond} - the heat transferred within the skin by conduction	III
q _{rad} - the heat exchange due to radiation to the wind tunnel (n) and to the model interior (m)	IV

 $q_{\rm bl}$ is the term we wish to determine for comparison with analytical predictions. To generate a "good" experiment, $q_{\rm bl}$ should be the dominant term.

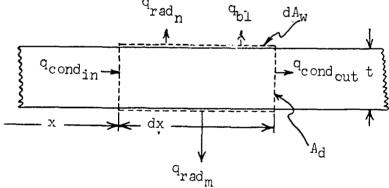


Figure 29 Energy Balance Notation

The general heat balance is written

$$q_{bl}dA_w + (q_{cond_{in}}A_{d_{in}} - q_{cond_{out}}A_{d_{out}}) - q_{rad}dA_w = q_{st}dA_w$$
 (11)

The temperature is assumed to be constant across the thickness of the surface - a condition referred to as the "thin-wall" assumption, i.e.,

$$T = \overline{T} = T_{W} \tag{12}$$

The heat conducted into an element of surface per unit time is

$$-k_m A_{\dim dx} = \frac{dT_w}{dx}$$
, and that out to $+k_m (A_d + \frac{dA_d}{dx} dx) (\frac{dT_w}{dx} + \frac{d^2T_w}{dx^2} dx)$.

Thus, the net rate of heat conducted into the element is

$$q_{cond_{in}} \Lambda_{d_{in}} - q_{cond_{out}} \Lambda_{d_{out}} - k_{m} \Lambda_{d} = \frac{d^{2}T_{w}}{dx^{2}} - dx - k_{m} \frac{d\Lambda_{d}}{dx} - \frac{dT_{w}}{dx} dx$$
 (13)

Also

$$dA_{W} = 1 dx$$
, $A_{cl} = tl$; (t 0.072-inch) (14)

The heat storage term may be written

$$q_{r,t}dt_{\mathbf{w}} = c_{\mathbf{p}_{\mathbf{m}}} d\mathbf{w} \frac{d\mathbf{w}}{d\mathbf{v}} \tag{15}$$

where dW is the element of mass lying beneath the surface area ${\rm d} A_{\rm W}.$ For a tabiform wall thickness

$$dW - \rho_{\text{in}} l dx t \tag{16}$$

It is possible to obtain reasonable, but not precise, estimates of the radiation heat fluxes. Radiation losses to the test section walls and nozzle blocks must be considered. Radiant energy impinging on the rear face of the test surface which criginates inside of the model (i.e., the support plate) is also of importance. The radiation heat exchange between the test surface and the wind tunnel nozzle - nozzle box combination is given by

$$Q_{w-n} - F_{w-n} \wedge_{w} \in_{w-n} (T_{w}^{4} - T_{n}^{4})$$
(17)

The surface $\Lambda_{\rm W}$ is completely surrounded by the nozzle and is flat. It can be stated immediately that ${\rm F_{W-N}}=1$. The model surface area is small compared to the mean test surface - nozzle separation distance. The fraction of reflected radiation which returns to the model is small enough to be neglected. The interchange factor, $\epsilon_{\rm W-N}$, is then

$$\epsilon_{w-n} = \epsilon_w \epsilon_n; \ \epsilon_w \approx 0.2h, \ \epsilon_n \approx 0.5, \ \epsilon_{w-n} \approx 0.1$$

The massiveness of the nozzle blocks and the inch thick test section walls allowed the assumption that the nozzle temperature \mathbf{T}_n was equal to the room temperature during the brief 20 second runs.

The emissivity of the model surface was estimated to be 0.2/4 which is the value for iron at 100°F freshly rubbed with emery paper. As the test surface is aerodynamically heated by the external flow, it receives varying amounts of radiant energy from the support structure. In this case, the radiation geometry consists of two parallel, closely-spaced flat plates. As before

$$Q_{w-m} = F_{w-m} \Lambda_{w} \in_{w-m} (T_{w}^{L_{+}} - T_{m}^{L_{+}})$$
(18)

Again the geometric factor \boldsymbol{F}_{w-m} is unity. The interchange factor for two parallel walls is

$$\epsilon_{w-m} = \frac{1}{\frac{1}{\epsilon_{w}} + \frac{1}{\epsilon_{m}} - 1}, \quad \epsilon_{w} = \epsilon_{m} \approx 0.24$$

$$\epsilon_{w-m} \approx 0.1$$
(19)

Combining all elements of the heat balance results in

$$q_{l:1} = \rho_{m} e_{p_{m}} t \frac{dT_{w}}{d\tau} - k_{m} t \frac{d^{2}T_{w}}{dx^{2}} + \sigma \epsilon_{w-n} (T_{w}^{4} - T_{n}^{4}) - \sigma \epsilon_{w-m} (T_{w}^{4} - T_{m}^{4})$$

$$(20)$$

In view of Equation 20, the following is a discussion of the experimental technique:

The model temperature was preset by surrounding the model with solid $CO_2(T=-109.8^{\circ}F)$, prior to starting the tunnel. These runs were made during a typical Minnesota summer day such that the tunnel temperature averaged $80^{\circ}F$. Therefore, the initial temperature potential (190°F) was the same for all tests. When the model temperatures were stable and uniform, the wind tunnel was started. The dry ice was removed by the

tunnel starting blast. Model temperatures increased with time as a result of the convective heating process. Each term in Equation 20 is time dependent. Initially only the heat storage term and the model-nozzle radiation terms contribute. As time proceeds, the other terms increase in importance. The equilibrium situation occurs when term II reduces to zero, and the model is at the adiabatic wall (T_{aw}) condition.

The accuracy of the methods depends to a large extent on the frequency with which reliable thermocouple readings are recorded near the beginning of a run. Modification M24 of the Dymec DY-2010A Data Acquisition System provided 25 channel input continuously monitored at a precise rate of 5 channels per second. Taking data early in a run implies that no surface heat conduction corrections are necessary; a fact which greatly simplifies data reduction. The acrodynamic heat flux is then obtained for the isothermal surface temperature case, which is the most basic and easily specified case and the only case for which most heat transfer analyses apply.

Neglecting terms II and IV*, Equation 20 is written

$$q_{bl} = h(T_{aw} - T_w) = \rho_m c_{p_m} t \frac{dT_w}{dT}$$
 (21)

with h and T_{aw} held constant, and at τ = 0, T_{w} = T(0), Equation 21 yields the particular integral

$$\frac{T_{aw} - T_{w}}{T_{aw} - T(0)} = e^{\frac{-hv}{\rho_{m}c_{p_{m}}t}}$$
(22)

The maximum radiant heat flux was found to be 10 Btu/ft²-hr. Since the initial temperature was 190° F, the radiation heat transfer coefficient of 10/190 = 0.05, was at most, 1/h percent of the convective heat transfer coefficient and could be safely neglected.

The left side of Equation 22 represents the ratio of the temperature potential remaining after τ seconds to the initial temperature potential. For small values of time ($\tau \approx 0$), Equation 23 may be written

$$\frac{T_{\mathbf{w}} - T(0)}{T_{\mathbf{a}\mathbf{w}} - T(0)} = \frac{h\tau}{\rho_{\mathbf{m}} c_{\mathbf{p}_{\mathbf{m}}} t}$$
(23)

Writing Equation 22 for two times, $\tau_{\rm l}$ and $\tau_{\rm 2}$ yields

$$h = \frac{\rho_{m} c_{p_{m}}}{(\tau_{2} - \tau_{1})} \cdot \ln_{e} \frac{T_{aw} - T_{w_{1}}}{T_{aw} - T_{w_{2}}}$$
(24)

Equation 24 was used in the actual data reduction procedure since the quantities T_{w_1} , T_{w_2} , and the time difference $(\tau_2 - \tau_1)$, are known somewhat more accurately than T_w , T(0) and the absolute time τ_1 - as required by Equation 22 . The indicated heat transfer coefficients obtained using Equation 24 were extrapolated to the condition of constant surface temperature, $(\tau=0)$, by plotting h versus the consumed temperature potential ratio $(T_{ave}-T(0))/(T_{aw}-T(0))$. This ratio is equal to zero when $\tau=0$.

The analysis of a sample run is presented in Figures 30 through 33. The temperature traces, the basic raw data, are given in Figure 30. The initial time, $\tau=0$, is found by inspection. The variation of heat flux, q_{bl} , with surface location is directly proportional to the trace slopes since the product, $\rho_m c_{p_m} t$, is the same for all positions.

^{*}The specific heat does vary strongly with temperature. In Figure 31 heat capacity data for pure iron is presented which should apply closely to the present material, type 304 stainless steel.

The stagnation point heat transfer rates are seen to be the smallest of the group while the slot rates are the largest. Heat transfer coefficients obtained by repeated application of Equation 24 are given in Figure 32 together with a visual representation of the effects of extrapolating to a uniform wall temperature condition. Experimentally, there seems to be a time-temperature region in which conduction effects are small enough to be ignored. This region does not include the slot where large gradients in temperature are rapidly established.

Finally, Figure 33 illustrates the integration of the local heat transfer values - a process which yields the one average heat transfer coefficient for the run.

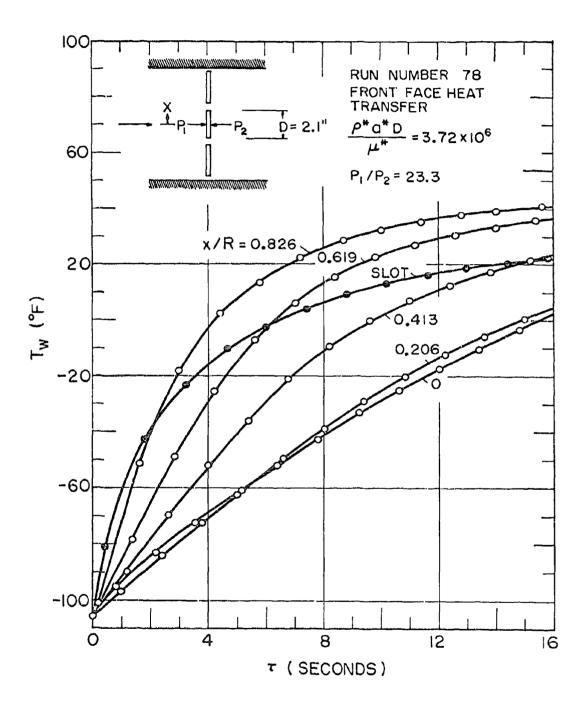


FIGURE 30. TYPICAL TEMPERATURE TRACES

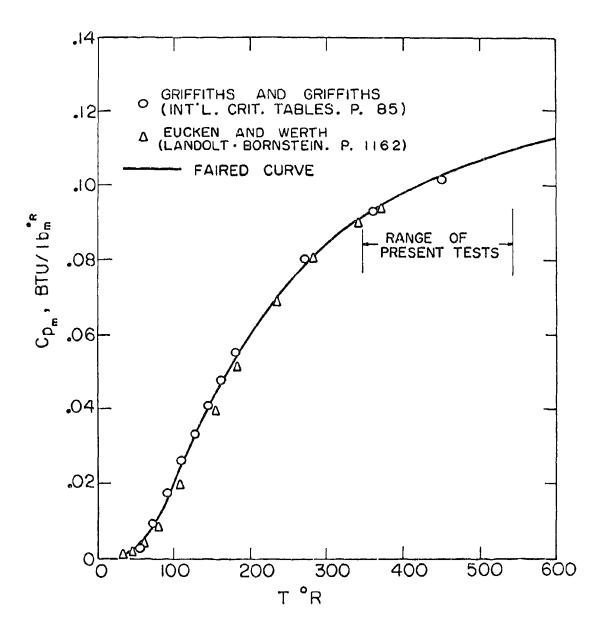
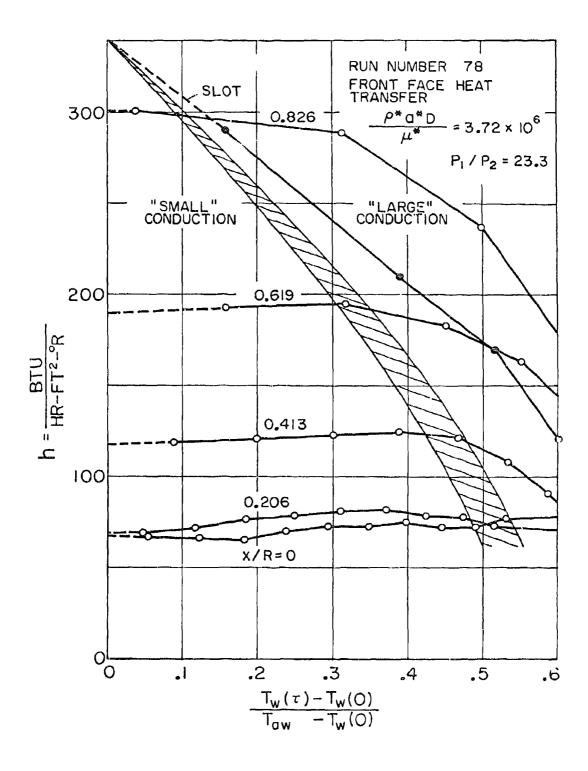


FIGURE 31. CORRELATION OF HEAT CAPACITY DATA FOR IRON



EIGURE 32. EXTRAPOLATION OF HEAT TRANSFER COEFFICIENTS TO A UNIFORM WALL TEMPERATURE CONDITION

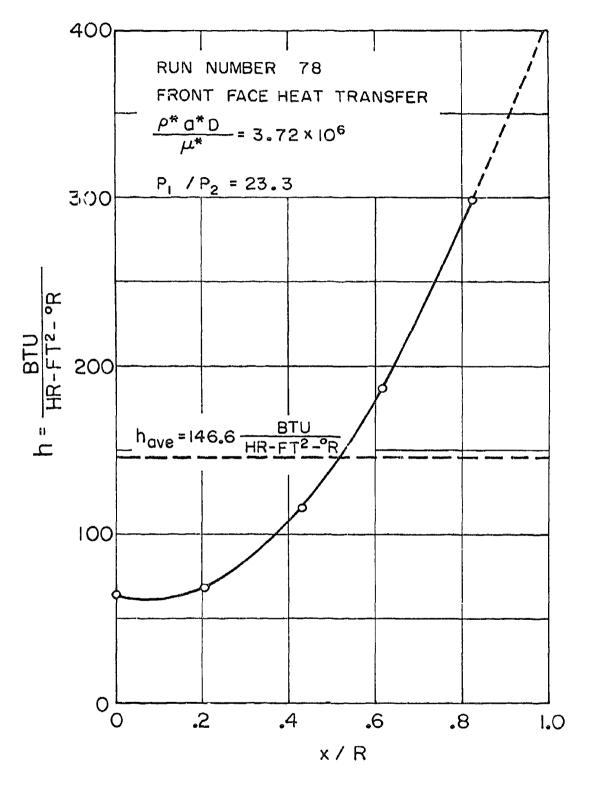


FIGURE 33. INTEGRATION OF THE LOCAL HEAT TRANSFER VALUES

DOCUMENT CONTROL DATA - R&D (Security classification of title, body of abstract and indexing annotation must be entered when the overall report is classified)							
1. ORIGINATING ACTIVITY (Corporate author)		28. REPORT SECURITY C LASSIFICATION					
University of Minnesota		Unclassified					
Institute of Technology	Ţ.	26 GROUP	<u>,</u>				
Mechanical Engineering Dept. Minneapolis, Minnesota 55455			n/a				
Experiments on the Thermal Performance of Ribbon Parachutes							
4. DESCRIPTIVE NOTES (Type of report and inclusive dates) Final Report July 1963 - September 1964							
5. AUTHOR(S) (Last name, first name, initial)							
Scott, C. J. Eckert, E. R. G.							
6. REPORT DATE	74. TOTAL NO. OF PA	GES	7b. NO. OF REFS				
May 1965	66		18				
Se. CONTRACT OR GRANT NO. Contract AF33(657)-11688	94. ORIGINATOR'S REPORT NUMBER(S) AFFDL-TR-64-192						
b. PROJECT NO. 6065							
c Task No. 606503	9 b. OTHER REPORT NO(S) (Any other numbers that may be assigned this report)						
d.	HTL-TR No. 61						
10. AVAILABILITY/LIMITATION NOTICES							
Qualified requesters may obtain copies of this report from DDC. Foreign announcement and dissemination of this report is not authorized. DDC release to OTS is not authorized.							
11. SUPPLEMENTARY NOTES	12. SPONSORING MILITARY ACTIVITY						
/a	Air Force Flight Dynamics Laboratory						
n/a	Research and Technology Division Wright-Patterson AFB, Ohio						

13. ABSTRACT

Experimental heat transfer studies were conducted on full scale ribbons of flat circular type parachutes having a geometric porosity of 20.5 percent. A pressurized subsonic wind tunnel served as the flow facility. The average approach flow velocity was 134 feet per second. The measurements were made in the Reynolds number range of one million to ten million, where the Reynolds number is based on the ribbon width of 2.1 inches and on the velocity and temperature of the flow in the slots between the ribbons. The pressure ratio applied to the ribbon was varied from 1.4 to 26.3. Using a transient energy balance, local and average heat transfer data were obtained and compared with available analyses.

KEY WORDS	LINKA		LINKB		LINK C	
	ROLE	wı	ROLE	ψT	HOLL	WT
Heat Transfer Ribbon Parachutes Wind Tunnel Investigations Pressure Distribution Aerodynamic Heating						

INSTRUCTIONS

- 1. ORIGINATING ACTIVITY: Enter the name and address of the contractor, subcontractor, grantee, Department of Detense activity or other organization (corporate author) issuing the report.
- 2a. REPORT SECURITY CLASSIFICATION: Enter the overall security classification of the report. Indicate whether "Restricted Data" is included. Marking is to be in accordance with appropriate security regulations.
- 2b. GROUP: Automatic downgrading is specified in DoD Directive 5200,10 and Armed Forces Industrial Manual. Enter the group number. Also, when applicable, show that optional markings have been used for Group 3 and Group 4 as authorized.
- 3. REPORT TIPLE: I have the complete report title in all capital letters. Titles in all cases should be unclassified. If a meaningful title cannot be selected without classification, show title classification in all capitals in parenthesis immediately following the title.
- 4. DESCRIPTIVE NOTES. If appropriate, enter the type of report, e.g., interim, progress, summary, annual, or final. Give the inclusive dates when a specific reporting period is covered.
- 5. AUTHOR(S): Enter the name(s) of author(s) as shown on or in the report. Enter test name, first name, middle initial, finditiary, show rank or thrench of service. The name of the principal author is an absolute minimum requirement.
- b. REPORT DATE: Enter the date of the report as day, month, year, or month, year. If more than one date appears on the report, use date of publication.
- 7a. TOTAL NUMBER OF PAGES: The total page count should follow normal pagination procedures, i.e., enter the number of pages containing information.
- 76. NUMBER OF REFERENCES: Enter the total number of references cited in the report.
- 8a. CONTRACT OR GRANT NUMBER: If appropriate, enter the applicable number of the contract or grant under which the report was written.
- 8b, 8c, & 8d. PROJECT NUMBER: Enter the appropriate military department identification, such as project number, subproject number, system numbers, task number, etc.
- 9a. ORIGINATOR'S REPORT NUMBER(S): Enter the official report number by which the document will be identified and controlled by the originating netivity. This number must be unique to this report.
- 9b. OTHER REPORT NUMBER(5): It the report has been assigned any other report numbers (either by the originator or by the sponsor), also enter this number(s).
- AVAILABHLTY/LIMITATION NOTICES: Enter any limutions on further discemination of the report, either than those

imposed by security classification, using standard statements such as:

- "Qualified requesters may obtain copies of this report from DDC."
- (2) "Foreign announcement and dissemination of this report by DDC is not authorized."
- (3) "U. S. Government agencies may obtain copies of this report directly from DDC. Other qualified DDC users shall request through
- ⁴U. S. military agencies may obtain coptes of this report directly from DDC. Other qualified users shall request through
- (5) "All distribution of this report is controlled. Qualified DDC users shall request through

If the report has been furnished to the Office of Technical Services, Department of Commerce, for sale to the public, indicate this fact and enter the price, if known.

- 11. SUPPLEMENTARY NOTES: Use for additional explana-
- 12. SPONSORING MILITARY ACTIVITY: Enter the name of the departmental project office or laboratory sponsoring (paring for) the research and development. Include address:
- 13 ABSTRACT. Enter an abstract giving a brief and factual summary of the document indicative of the report, even though it may also appear elsewhere in the body of the technical report. If additional space is required, a continuation sheet shall be attached.

It is highly desirable that the abstract of classified reports be unclassified. Each paragraph of the abstract shall end with an indication of the military accurity classification of the information in the paragraph, represented as (TS), (S), (C), or (U)

There is no limitation on the length of the abstract. However, the suggested length is from 150 to 225 words.

14. KEY WORDS: Key words are technically meaningful terms or short phrases that characterize a report and may be used as index entries for cataloging the report. Key words must be selected so that no security classification is required. Identifiers, such as equipment model designation, trade name, military project code name, geographic location, may be used as key words but will be followed by an indication of technical context. The assignment of links, rules, and weights is optional.